

Authors' Response to the Comment of Referee #1

We thank Referee #1 for his detailed review and his suggestions for improvement.

Referee #1 identified two major problems.

- 1) It is unlikely that the small-scale wave structures we observe are gravity waves. They should rather be considered as instability features.
- 2) Our values of K and ϵ are too high and he doubts whether our approach of a rotating cylinder is the correct model for our turbulence observations.

Passages in red have been deleted or rephrased as indicated.

Referring to major problem 1):

We revised the discussion of our observed wave structures and switched to focus of our interpretation from gravity waves to instability features. The word 'wave' we use for convenience refers to wave-like features as seen in the images. We introduced section 4.1 with "We inserted the passage "Please note that we are using the word 'wave' for all wave-like structures we find in the images. The question whether these are actual gravity waves is discussed in section 5." at the beginning of section 4.1." to clarify this.

Referee #1 doubted that any significant portion of our observed structures with horizontal wavelengths below 5 km would be gravity waves. He gave multiple reasons why these structures would rather be instability features of gravity waves. We agree with his detailed explanations and refrain from considering wave structures with periods above the BV period gravity waves. As Referee #1 states correctly, Doppler-shifting may play a vital role and we have no systematic wind data to account for that.

We omitted the distinction between waves above and below the BV period in Figure 1. Consequently, also the sentence "The contribution of wave events with a period longer than the respective BV period is coloured in grey." disappeared in the caption of Figure 1. We updated the wording and the statistical values in section 4.1 (results: statistics of wave parameters) Lines 165 ff. resulting from this.

*"Instability features are blown by the wind. GWs in general do not travel in the wind direction. But when they do two effects occur that make them **less likely to be observed** in the airglow layer. They are both related to the **dispersion relation** that shows that as the intrinsic velocity (the velocity with respect to the background wind) approaches the wave velocity the vertical wavelength decreases because the intrinsic frequency becomes small. This causes two effects.*

*Unless the intrinsic frequency is very close to the BV frequency the vertical wavelength will be less than the horizontal wavelength. Now for the waves that are presented in this paper the **vertical wavelength will be 4.5 km or much smaller**. GWs that have wavelengths thinner than the airglow layer (8-10 km) will suffer phase cancellation and will have vastly reduced amplitudes and likely will be difficult to see (Swenson and Liu, 1998).*

As the vertical wavelength decreases the waves undergoes viscous dissipation and instability formation. This is discussed somewhat in Hecht et al., 2000 as well in Hecht et al., 2018. For

*the former and assuming the very large viscosity implied by the current work GW, lifetimes could be seconds to a few minutes for the GWs in this study. Related to b is that if the features are really blown by the wind they are at a critical level and **probably do not survive**. I should note that waves in this study are travelling at a very low speed so it is very **likely that extremely common wind variations would exceed the wave speed and the critical level interaction (viscous dissipation or instability formation) would occur**. Hence, it seems very unlikely these are GWs.”*

We agree with this detailed discussion of the dispersion relation.

We added ‘If Figure 3b was the phase speed distribution of gravity waves, it is likely that a majority of them would encounter critical levels somewhere and would not be observable in the OH* layer.’ to the discussion.

“The characteristics of these waves if they are GWs, as currently presented, seem strange. Their phase speeds are quite low-below 20 m/s. GW climatology’s typically show phase speeds of up to 50 m/s with the histogram of speeds centered closer to 40 m/s.”

We included this point in the discussion.

Line 360ff: “The quite slow phase speeds (mean value 13.3 m / s) are one hint for this as typical gravity wave phase speeds accumulate around 40 m / s (see, e.g., Wachter et al., 2015 and Wüst et al., 2018).”

“I was somewhat curious on how the monochromatic wavelengths were derived. They state they use a 2D FFT. Now FFTs assume the wave is present over the whole field of view and are often a little misleading with respect to monochromatic waves for airglow images because waves may be present over only a small fraction of the field. In the Hannawald reference they give a very nice image showing waves and I believe the FFT approach should be appropriate for data like that. But to date, while small scale instabilities have been identified with horizontal wavelength of a few to ~10 km there have been no reports of GWs with horizontal wavelengths of 5 km to 0.05 km. I would like to see images with their respective FFTs for images where the wavelengths are ~ 4 ,1,0.5,0.1 and 0.05 km. I am wondering if most of those images show features that resemble OH images (shown in the Hecht references) with instability features and their associated secondary instabilities and the resulting turbulences. I am really curious about GWs (or even instabilities/wave trains) with wavelengths at or much below ~500 m. These have not been reported before.”

We have not found waves with horizontal wavelengths down to 0.05 km, but this is the short-scale limit of our analysis, corresponding to twice the spatial resolution of $2 \times 24 \text{ m} = 48 \text{ m}$.

It is true that assuming stationarity the 2D-FFT rather finds wave structures that extend over the entire image. We have added a sample image of the smallest structure we found with a horizontal wavelength of ca. 1.9 km with its 2d spectrum (new Figure 1) and it does extend over at least half of the image.

In fact, we observed and reported a small “wave-like” instability feature with a horizontal wavelength of 550 m several years ago (see Sedlak et al., 2016). However, we doubt that such a small wave packet of limited spatial extension would appear in the 2D-FFT. A 2-dimensional wavelet analysis could account for such non-stationary features in future work.

Referring to major problem 2):

Considering the referee's extensive argumentation, we agree that assuming a rotating cylindrical model, as we did, exhibits several weaknesses. Demanding a perfect rotating cylinder is a very strong assumption that may apply to some of the turbulent vortices, but definitely not to all of them. As Referee #1 states correctly, there are several non-cylindrical vortices besides the rotation cylinder in our example in Figure 3 and there is no particular need for a rotating model. Furthermore, we agree that using climatological values of N for our quite short-time and localized episodes is relatively coarse.

We decided to follow his advice and adapted the method of Hecht et al. (2021) following Chau et al. (2020). We refrained from determining K from a rotating cylinder model. Instead, we read the feature size L and the residual velocity v_{res} from the image series and directly calculated ε by using the equation $\varepsilon = C \frac{v_{res}^3}{L}$ with $C \approx 1$ (Hecht et al., 2021). As Referee #1 assumed correctly, this was not always easy for all our examples. Staying with the episodes where the derivation of ε was possible with this method, our data basis reduced from 45 to 25 episodes. This changed the results of our correlation analysis with gravity wave activity: We now hardly see any significant correlation with the activity of gravity waves between 6 and 480 min.

Although the values are now a bit lower (the rotating cylinder model certainly served as an upper boundary value since it assumed maximum mixing; Referee #2 stated this quite correctly) some of them still exceed the limit of 1 W/kg with the maximum being 9 W/kg. We provide a careful discussion of the deviations from previous studies.

As the derivation of ε is quite difficult and due to the variety of turbulent episodes we furthermore decided to show more of our turbulent observations. Besides our former video supplement from 4 November 2018, we now present three more video sequences.

Changes made in the manuscript:

Abstract

Lines 14, 38, 49, 55, 72, 77, 108, 186, 264, 269, 272, 279, and 312: We put commas before and behind "e.g."

Line 16f: Added "instability features from breaking secondary waves"

Line 17: Replaced "originating from breaking primary waves" by "that were created" and dropped "(westward)" and "(summer)".

Line 20f: We changed "Furthermore, observations of turbulent vortices allowed the estimation of eddy diffusion coefficients in the UMLT from image sequences in 45 cases. Values range around $10^3 - 10^4 \text{ m}^2\text{s}^{-1}$ and mostly agree with literature. Turbulently dissipated energy is derived taking into account values of the Brunt-Väisälä frequency based on TIMED-SABER (Thermosphere Ionosphere Mesosphere Energetics Dynamics, Sounding of the Atmosphere using Broadband Emission Radiometry) measurements as presented by Wüst et al. (2020). Energy dissipation rates range between 0.63 W kg^{-1} and 14.21 W kg^{-1} leading to an approximated maximum heating of

0.2-6.3 K per turbulence event. These are in the same range as the daily chemical heating rates reported by Marsh (2011), which apparently stresses the importance of dynamical energy conversion in the UMLT.”

to

“We present multiple observations of turbulence episodes captured by our high-resolution airglow imager and estimated the energy dissipation rate in the UMLT from image sequences in 25 cases. Values range around 0.08 and 9.03 $W kg^{-1}$ and are higher than those in recent literature. The values found here would lead to an approximated localized maximum heating of 0.03-3.02 K per turbulence event. These are in the same range as the daily chemical heating rates for the entire atmosphere reported by Marsh (2011), which apparently stresses the importance of dynamical energy conversion in the UMLT.”

Introduction

Line 40: We changed “ground” to “troposphere”

Lines 54ff: We changed

“They cause turbulent mixing of the medium, which is described by the eddy diffusion coefficient K . K can be calculated from the eddy radius r_e and the circumferential velocity v_e by

$$K = \frac{2}{3\pi} r_e v_e \quad (1)$$

(see e.g. Prölss, 2001. The derivation is outlined in detail in appendix A.). According to Weinstock (1978), knowing K and the BV frequency N , an estimate for the energy dissipation rate ϵ - the rate at which turbulent kinetic energy is dissipated into heat at the short-scale end of the energy cascade of the inertial subrange (Li et al., 2016) - can be calculated using

$$K \approx 0.81 \cdot \left(\frac{\epsilon}{N^2}\right). \quad (2)$$

to

“They cause turbulent mixing of the medium, resulting in the dissipation of turbulent energy at an energy dissipation rate ϵ . According to the theory of stratified turbulence, ϵ depends on the characteristic length scale L and velocity scale U of the turbulent features. The energy dissipation rate is then given by

$$\epsilon = C_\epsilon \frac{U^3}{L} \quad (1)$$

(see, e.g., Chau et al, 2020; who apply this equation to radar observations of KHIs). C_ϵ is a constant which is found to be equal to 1 (Gargett, 1999).”

Lines 70ff: We changed

“This is why turbulence investigations in the UMLT are challenging and there are only few values of K available at UMLT heights. Lübken et al. (1997) use rocket measurements to retrieve K and ϵ in the height range 65-120 km. Liu (2009) presents a method for the estimation of K from gravity wave momentum fluxes derived from lidar data. Baumgarten & Fritts (2014) use imaging techniques of mesospheric noctilucent clouds to investigate the formation of KHIs and the onset of turbulence.”

to

“This is why turbulence investigations in the UMLT are challenging and there are only few values of ϵ available at UMLT heights. Lübken et al. (1997) use rocket measurements to retrieve ϵ in the height range 65 - 120 km. Baumgarten & Fritts (2014) use imaging techniques of mesospheric noctilucent clouds to investigate the formation of KHs and the onset of turbulence.”.

Line 76: We changed “These include...” to “Remote sensing techniques include...”

Line 83: We changed “Proceedings” to “Improvements”

Data Basis

Line 138: We inserted “...from the input images...” during the 2d-FFT”.

Line 156: We inserted “An exemplary event and the respective 2-dimensional spectrum are shown in Figure 1. We often observe episodes of turbulence in our image series that exhibit the typical dynamics of vortex formation and quasi-chaotic behavior.”

Line 164: Replaced “45” by “25” and “vortex” by “turbulence”

Lines 166ff: Omitted “For both, gravity wave statistics (section 4.1) and the calculation of the energy dissipation rate (section 4.2) the BV frequency is required, which is adapted from the climatology presented by Wüst et al. (2020). It is based on TIMED-SABER (Thermosphere Ionosphere Mesosphere Energetics Dynamics, Sounding of the Atmosphere using Broadband Emission Radiometry) temperature data and takes into account the seasonal variability of the angular BV frequency. The climatology of the grid point (45° N, 10° E) is used, which is closest to our FOV. Depending on the day of the year (DoY) the BV frequency is given by

$$N = 2.20 \cdot 10^{-2} \text{s}^{-2} + 0.19 \cdot 10^{-2} \text{s}^{-2} \sin\left(\frac{2\pi}{324.51 \text{d}} \cdot \text{DoY} - 2.02\right) + 0.05 \cdot 10^{-2} \text{s}^{-2} \sin\left(\frac{2\pi}{180.00 \text{d}} \cdot \text{DoY} + 1.61\right). \quad (3)$$

We use an uncertainty of $\pm 5\%$ as according to Wüst et al. (2020) 91% of their data lie within this range around the harmonic approximation. The BV period is then referred to as $\tau_{BV} = \frac{2\pi}{N}$.”

Results

We inserted the passage “Please note that we are using the word ‘wave’ for all wave-like structures we find in the images. The question whether these are actual gravity waves is discussed in section 5.” at the beginning of section 4.1.

Line 165 ff: We dropped “For each wave event the individual BV period is calculated based on Eq. (3) and the DoY. Ca. 63% of the observed wave events have a period longer than the respective BV period and will be referred to as gravity wave events in the following. Their statistical contribution is highlighted in grey in **Fehler! Verweisquelle konnte nicht gefunden werden.**”

Line 168 f: We dropped “The median value of gravity wave periods is found at 517 s (8.6 min).”.

Line 169: 17.6 m/s changed to 139.8 m/s; 7.9 m/s changed to 13.3 m/s

Line 170: 3.3 m/s changed to 10.3 m/s. 50.7 % (49.3 %) changed to 52.7 % (47.3 %). Dropped the word “gravity”.

Line 171: Dropped the word “gravity”.

Line 172: 5.4 m/s (5.3 m/s) changed to 9.4 m/s (8.2 m/s). 3.0 m/s (3.1 m/s) changed to 8.9 m/s (7.4 m/s).

Line 173: 53.8 % changed to 56.0 %. 46.2 % changed to 44.0 %.

Line 174: 47.9 % changed to 49.5 %.

Line 175: 52.1 % changed to 50.5 %. 44.4 % (53.5 %) changed to 42.0 % (55.7 %).

Line 176: 4.7 m/s (5.3 m/s) changed to 7.5 m/s (9.4 m/s).

Line 177: 3.0 m/s (3.2 m/s) changed to 7.1 m/s (8.7 m/s).

Lines 192 ff: We added: “To give an impression of the turbulent dynamics we observe, we present four of our turbulence episodes as video supplement. On 16 November 2017, 02:16 UTC, the turbulent breakdown of parts of an extended wave field can be observed (video 1). On 6 December 2017, 00:26 UTC, several fronts seem to be building up and form rotating vortices (video 2). This can be observed even clearer on 14 October 2018, 17:08 UTC, where the residual movement of turbulent features can be well recognized above the general background movement (video 3). On 4 November 2018, 19:18 UTC, breaking wave fronts seem to form rotating structures of nearly cylindrical shape, while these are accompanied by other turbulently moving eddies (video 4).

We estimate the turbulent energy dissipation rate ϵ using equation (1). However, in contrast to Chau et al. (2020) who used radar measurements, we only have horizontal information from our airglow imager. Hecht et al. (2021) demonstrate an approach how to apply equation (1) to purely horizontal airglow imager data, which we adapt to our observations in the following. The characteristic length scale L can be read from the images by measuring the size of the turbulent features. The velocity scale is given by the residual velocity v_{res} of these features. In our observations, they are part of larger instability features, which we assume to be advected by the background wind. We determine v_{res} by reading the actual velocity of the turbulent features and subtracting the background movement v_{bg} in the resulting direction. This is exemplarily shown in Figure 4. The two patches highlighted therein are both moving to the upper right direction but are approaching each other. This helps distinguishing background and residual movement.”

and dropped:

“The eddy parameters needed for the calculation of the eddy diffusion coefficient (Eq. 1) are determined manually from the image series of the 45 observations of turbulence. It has to be kept in mind that we are deriving properties of a three-dimensional movement from two-dimensional data.

We assume the vortices to rotate in a perfect circular shape. The lateral expansion creates the impression of a rotating cylinder. Coherently moving structures give indication of the horizontal velocity vector. Unless the rotational axis is aligned perpendicular to the image plane, the three-dimensional vortex rotation manifests as more than one coherent structure that is moving against or overtaking each other (see e.g. Sedlak et al., 2016; Figure 6 therein). During data inspection we

noticed that the orientation of the rotational axis can be aligned in any direction. It tends to be parallel to the image plane when it evolves directly from the crests of a breaking wave. However, we could also observe eddies rotating around an axis aligned almost perpendicular to the image plane. An example of a rotating vortex within a FAIM 3 snapshot on 4 November 2018 at 19:36:41 UTC is displayed in Figure 3a. The rotational axis and the direction of rotation are marked therein and on an actual cylinder (Figure 3b) for clarification. Since it is very difficult to identify a vortex structure in a single picture we have attached a video sequence of this episode (Video 1). The vortex radius and velocity are read from the images. Besides measuring the vortex rotation, it has also to be taken care of the overall image: if additional to the eddy movement all structures in the FOV are moving into a common direction, this background motion has to be subtracted. In the example shown above the vortex is advected toward the left corner. The distance between camera and observed vortex is much larger than the expansion of the vortex along the rotation axis so that falsifications arising from different perspectives of the vortices can be neglected. This principle is illustrated in Figure 4. As the vortices are three-dimensional the alignment of the rotational axis should not affect the value of the vortex parameters in the images: it does not matter if the axis is aligned perpendicular, parallel or in any other angle to the image plane, the vortex size will be accessible from the two-dimensional projection of the image assuming circular eddy movement. The same holds for the circumferential velocity since both the radius and the circulation time remain unchanged. However, perfectly circular eddy rotation does not necessarily occur in nature. Deviations from circularity can lead to both over- and underestimation of vortex sizes depending on the vortex orientation. Since isotropy is one of the characteristic properties of turbulent movements one may presume that from a statistical point of view both cases occur equally so that no systematic error is made.”

Lines 232ff: We changed

“As stated in section 3 we found 45 episodes of turbulence that allowed the derivation of the vortex radius and circumferential velocity. The resulting eddy diffusion coefficients K are shown in **Fehler! Verweisquelle konnte nicht gefunden werden.** We assume a general read-out error of ± 3 pixels, which corresponds to a distance of ± 72 m. The circumferential velocity is determined by reading the distance a patch on the rotating cylinder surface covers within an episode of at least ten images, which corresponds to a time span of 28 s. Thus, the circumferential velocity is estimated with an error of ± 2.6 m s^{-1} . The arising uncertainties of K are calculated following the rules of error propagation.

The values of K range from 0.12 to $1.94 \cdot 10^4$ m^2s^{-1} . The mean value is $0.76 \cdot 10^4$ m^2s^{-1} ”

to

“As stated in section 3 we found 25 episodes of turbulence that allowed the derivation of L and v_{res} . Using equation (1), the energy dissipation rate is then calculated by $\epsilon = \frac{v_{res}^3}{L}$. The resulting values are shown in **Fehler! Verweisquelle konnte nicht gefunden werden.** We assume a general read-out error of ± 3 pixels, which corresponds to a distance of ± 72 m. Velocities are determined by reading the distance a feature covers within an episode of at least ten images, which corresponds to a time span of 28 s. Thus, velocities are estimated with an error of ± 2.6 m s^{-1} . The arising uncertainties of ϵ are calculated following the rules of error propagation.

The values of ϵ range from 0.08 to 9.03 W kg^{-1} . The median value is 1.45 W kg^{-1} ”

Lines 240ff: We dropped

“(standard deviation of $0.53 \cdot 10^4 \text{ m}^2\text{s}^{-1}$) and we retrieve a median of $0.59 \cdot 10^4 \text{ m}^2\text{s}^{-1}$. It is difficult to exactly quantify the error of manual parameter determination from the images. However, in this work we rather focus on the order of magnitude of K . When calculating K two distance values are read from the images (one for the vortex size and one for the determination of the circumferential speed). Considering Eq. (1), a mistake of factor 10 is made for K if these distances are misread by a factor of at least $\sqrt{10}$. The shortest (and therefore most difficult to determine) diameter in our analysed examples was 768 m. For an error of one order of magnitude of K this distance must be misread as either shorter than 243 m or longer than 2428 m, i.e. a distance of 32 pixels must be wrongly interpreted as shorter than 9 pixels or longer than 101 pixels. This lies far beyond the read-out uncertainty of ± 3 pixels we introduced above and can be assumed to be much worse than any read-out error one would normally make.

The energy dissipation rate ϵ can be estimated from the eddy diffusion coefficient K according to Eq. (2) using the BV frequency as described by Eq. (3).

As can be seen in **Fehler! Verweisquelle konnte nicht gefunden werden.** the energy dissipation rate of the observed turbulence events is in the range $0.63 - 14.21 \text{ W kg}^{-1}$.”

Line 254: We updated “146 s” to “241 s” and “2.4” to “4.0”.

Line 258: We updated “220” to “30” and “6346” to “3015”.

Line 262: We updated “0.2-6.3 K” to “0.03-3.02 K” and dropped “64% (21 out of 33) of these values are larger than one Kelvin.”

Line 268: We inserted a missing “o”

Lines 277ff: We changed “We find a slight but significant anticorrelation for gravity wave periods in the range 122 - 207 min. For these periods the mean value of the correlation coefficient is -0.46. The highest coefficient of anticorrelation is -0.52 at a period of 178 min. ”

to

“We find almost no significant correlation for any gravity wave period.”

Discussion:

Line 280: We replaced “The directions of propagation are quite uniformly distributed over all quadrants as can be seen in Figure 2” by “As can be seen in Figure 3, the wave structures we observed exhibit multiple directions.”

Line 288: We replaced “(positive zonal phase speed) and in westward direction during summer. Although this tendency is quite weak,” by “whereas zonal directions are quite balanced during summer. Although the eastward tendency during winter is quite weak,”.

Line 290: We added “tropospheric and”.

Lines 292ff: We replaced “The reversed stratospheric winds during summer would consequently allow some more eastward travelling gravity waves to propagate upward (see e.g. Hoffmann et al., 2010; Hannawald et al., 2019). Since the highest observed phase speed of waves with periods longer than the BV period is only 17.6 m s⁻¹, it can be assumed that in the majority we do not observe gravity waves that are originating from low altitudes and are fast enough not to be blocked by the stratospheric wind fields.”

by

“During summer the stratospheric winds reverse to westward direction, so that eastward oriented gravity waves are filtered in the tropopause and westward oriented gravity waves are filtered in the stratosphere (see, e.g., Hoffmann et al., 2010; Hannawald et al., 2019).”

We inserted

“As we have no accompanying wind measurements in the height of our observations it is difficult to decide by means of the period whether the wave structures presented in section 4.1 are small-scale gravity waves or instability features. Ca. 63 % of the observed wave events have an observed period above the BV period (here we used the climatology presented by Wüst et al., 2020), however these could also be Doppler-shifted instability features instead of gravity waves. While the distinction between largely extended wave-fields (bands) and small localized wave structures that are related to instability (ripples) is often made at a horizontal wavelength of 10 - 20 km (Taylor et al., 1997; Nakamura et al., 1999), Li et al. (2017) remark that even structures with horizontal wavelengths of 5 - 10 km may sometimes be gravity waves rather than instability features.”

after this passage.

Line 302 ff: We changed “Considering the directional distribution, it is possible that the major part of our waves may” to “If this would be true for our small-scale wave structures, they might rather”.

Line 321 f: We changed “southward in 62 % of cases.” to “southward in 71 % of cases.”.

We inserted

“However, regarding the small horizontal wavelengths below 4.5 km, it is more likely that the major part of the observations presented in section 4.1 are related to instability features. The quite slow phase speeds (mean value 13.3 m / s) are one hint for this as typical gravity wave phase speeds accumulate around 40 m / s (see, e.g., Wachter et al., 2015 and Wüst et al., 2018). If Figure 3b was the phase speed distribution of gravity waves, it is likely that a majority of them would encounter critical levels somewhere and would not be observable in the OH* layer.”

after this passage.

Line 371 ff: We replaced “Li et al. (2017) report that ripples are hard to distinguish from small-scale gravity waves. Height-resolved measurements of the horizontal wind would be needed to determine the local wind shear and make a profound statement about atmospheric instability. Nevertheless,”

by

“Considering the fact that the directional peculiarities of our observed wave events fit well with the expected behavior of secondary gravity waves, as discussed above, support the scenario of the wave structures being ripples from dynamic instabilities of secondary gravity waves, that originate from the stratospheric and mesospheric jet.”

We added

“Nevertheless, height-resolved measurements of the horizontal wind would be needed to determine the local wind shear and make a profound statement about atmospheric instability. It has to be kept in mind that a 2d-FFT was used. Thus, periodic structures are assumed to be stationary, i.e., they extend over the entire image. Faint structures that appear only in small parts of the image (as does for example the 550m wave packet in Sedlak et al., 2016; Fig. 2) would be underrepresented by this analysis.”

at the end of the discussion section of the wave statistics.

Lines 384ff:

We changed

“There are still very few measurements of turbulent eddy diffusion coefficients in the UMLT. Lübken (1997) reports K to be around $10^1 - 10^2 \text{ m}^2\text{s}^{-1}$ at a height of 87 km at high latitudes. Hodges (1969) states that the eddy diffusion coefficient caused by gravity waves is typically around $10^3 \text{ m}^2\text{s}^{-1}$. According to the CIRA (Committee on Space Research (COSPAR) International Reference Atmosphere) climatology of 1986 (NASA National Space Science Data Center, 2007) global values range between magnitudes of 10^2 and $10^3 \text{ m}^2\text{s}^{-1}$. LIDAR measurements above New Mexico, USA deliver values that vary strongly around a magnitude of $10^2 \text{ m}^2\text{s}^{-1}$ (Liu, 2009). Smith (2012) notes that the WACCM (Whole Atmosphere Community Climate Model) climatology exhibits rather small values with magnitude $10^1 \text{ m}^2\text{s}^{-1}$ and that the huge discrepancies of K estimates cannot be fully explained yet. The here-presented values of K exhibit a magnitude of $10^3 - 10^4 \text{ m}^2\text{s}^{-1}$, which partly agrees with recent results, although some of our values are higher.”

to

“Measuring the eddy diffusion coefficient in the UMLT is still challenging and there are only few studies yet. Rocket measurements of Lübken (1997) deliver energy dissipation rates between ca. 0.01 and 0.1 W kg^{-1} between 85 and 90 km height at high latitudes. Chau et al. (2020) find an energy dissipation rate of 1.125 W kg^{-1} for their KHI event observed in the summer mesopause and state that this a rather high value compared to the findings of Lübken et al. (2002). Hocking (1999) provides a rescaled overview of earlier values of the energy dissipation rate and these have a maximum magnitude of 0.1 W kg^{-1} . Hecht et al. (2021) derive a value of 0.97 W kg^{-1} from airglow images of a KHI event. Ranging from 0.08 up to 9.03 W kg^{-1} the values of energy dissipation rate derived here are higher than reported by other studies. However, the median value of 1.45 W kg^{-1} is not too far away from the values of Chau et al. (2020) and Hecht et al. (2021).”

Lines 402f: We added “– except for the studies of Hecht et al. (2021), whose value is quite similar to the median value of our data –,

Lines 405ff: We dropped “Nevertheless, the agreement of the above-mentioned authors on eddy parameters in the UMLT is quite good, considering the fact that energy dissipation rate in the upper troposphere and lower stratosphere varies by a factor of more than five orders of magnitude (Li et al., 2016).”.

Line 408: Changed “vortex” to “turbulence”

Line 409: Changed “Circumferential speed and vortex radius” to “The length scale and velocity scale of turbulent features”

Line 410: “and we” changed to “. We”

Lines 412f: Inserted “However, using equation (1) velocity dominates the length scale due to its power of 3, so that ϵ strongly depends on a parameter, which is quite difficult to extract from the images.”

Line 414: Dropped “eddy diffusion coefficient and”

Line 415: Replaced “eddy diffusion coefficients” by “energy dissipation rate” and replaced “significant anticorrelation” by “no significant correlation”

Lines 416: Changed “122-207 min” to “6-480 min”

Lines 416ff: Changed

“One may assume that turbulent vortices we observe could be predominantly attributed to breaking gravity waves in this period range. If this was the case, stronger wave breaking would manifest as higher eddy diffusion coefficients and result in a lower activity of gravity waves with periods 122-207 min in the UMLT. However, especially observations of period-resolved gravity wave activity at altitudes below would be needed to confirm this assumption.

Assuming that the turbulently dissipated energy is entirely converted into heat we find temperature changes of 0.2-6.3 K that occur within time spans of 2.4–15.4 min. Marsh (2011) report chemical heating rates in the atmosphere to be around 3–4 K per day. Given that our analysed episodes are typical representatives of turbulent wave breaking, dynamical heating by gravity wave dissipation would deliver the same effect within few minutes as does chemical heating during an entire day.”

to

“Turbulence thus cannot be related to distinct periods of the gravity wave spectrum with the here-presented data. Note that the spectrometer GRIPS is sensitive to much larger spatial scales than FAIM. A larger data basis of turbulence parameters and especially observations of period-resolved gravity wave activity at altitudes below will be needed to answer the question if all parts of the gravity wave spectrum drive turbulence generation in the UMLT equally.

Assuming that the turbulently dissipated energy is entirely converted into heat we find temperature changes of 0.03-3.02 K that occur within time spans of 4.0–15.4 min. Marsh (2011) report chemical heating rates in the atmosphere to be around 3–4 K per day. Given that our analysed episodes are typical representatives of turbulent wave breaking, dynamical heating by gravity wave dissipation

would deliver the same effect within few minutes at very localized areas in the UMLT as does chemical heating during an entire day for the whole atmosphere.”

Summary

Lines 429ff: We changed

“We present an analysis of small-scale wave dynamics from OH* imager data acquired between 26 October 2017 and 6 June 2019 at Otlica Observatory, Slovenia. Measurements have been performed with the imager FAIM 3, which has a spatial resolution of ca. 24 m pixel⁻¹ and a temporal resolution of 2.8 s.

Wave structures in the images are systematically identified by applying a 2d-FFT to nocturnal image sequences during clear sky episodes. All wave events meeting our persistency criteria were used to derive a statistical analysis of wave structures with horizontal wavelengths between 48 m and 4.5 km. 63% of the wave events have a period longer than the BV period and may be tentatively considered as gravity waves. We find an isotropic distribution of directions of propagation, which indicates that wave structures may be mostly created above the stratospheric wind fields. However, a weak seasonal dependency is found: zonal directions of wave propagation are slightly more eastward during winter and westward during summer. We speculate these to be generated by breaking gravity waves in the course of wind filtering, receiving their zonal direction through advection by the background wind. We find a stronger tendency of southward propagation during summer, which may point to a vital role of gravity wave filtering and excitation of secondary waves by the meridional mesospheric circulation. It is possible that secondary waves and instability features represent the majority of our observed waves.

Furthermore, we estimated turbulence parameters from 45 episodes of vortex observations. The derived values of eddy diffusion coefficients are in the range around $10^3 - 10^4 \text{ m}^2\text{s}^{-1}$ and agree mostly with earlier results from rocket and lidar measurements and simulations. Considering the respective values of the BV frequency as calculated by Wüst et al. (2020) we retrieve energy dissipation rates between 0.63 W kg^{-1} and 14.21 W kg^{-1} , that cause estimated heatings by 0.2 - 6.3 K per turbulence event. These have the same order of magnitude”

to

“We present an analysis of small-scale dynamics of instability features and turbulence from OH* imager data acquired between 26 October 2017 and 6 June 2019 at Otlica Observatory, Slovenia. Measurements have been performed with the imager FAIM 3, which has a spatial resolution of ca. 24 m pixel⁻¹ and a temporal resolution of 2.8 s.

Wave-like structures in the images are systematically identified by applying a 2d-FFT to nocturnal image sequences during clear sky episodes. All events meeting our persistency criteria were used to derive a statistical analysis of wave-like structures with horizontal wavelengths between 48 m and 4.5 km. The small horizontal scales are a strong hint that these are likely instability features of breaking gravity waves like ripples. We generally find variable directions of propagation, which indicates that these wave-like structures may be mostly created above the stratospheric wind fields. However, a weak seasonal dependency is found: zonal directions of propagation are slightly more eastward during winter and westward during summer. We speculate these to be instability features generated by breaking secondary gravity waves, receiving their zonal direction through advection by

the background wind. We find a stronger tendency of southward propagation during summer, which may point to a vital role of gravity wave filtering and excitation of secondary waves and their subsequent instability features by the meridional mesospheric circulation.

Furthermore, we observed and presented OH* imager observations of turbulence with high spatio-temporal resolution. We estimated turbulence parameters from 25 episodes of eddy observations. Following the approach of Hecht et al. (2021) we derived the energy dissipation rates for our observed events by reading the turbulent length and velocity scale from the image series. Our values range between 0.08 and 9.03 $W kg^{-1}$ and are higher than earlier rocket measurements. The values presented here would cause localized heatings of 0.03-3.02 K per turbulence event. The largest of these reach the same order of magnitude”

Appendix

We dropped Appendix A.

Figures

Figure 1 is now a sample event with its 2D-FFT spectrum.

Figure 2 (former Figure 1): Histograms of wave parameters without separation by the BV period

Figure 3 is now former Figure 2

Figure 4 (former Figure 3): New snapshot showing how to read the new wave parameters from the images.

Former Figure 4: dropped

Figure 5: Plot of temporal course and histogram of ϵ (no K values anymore)

Figure 6: Updated histogram of temperature changes

Figure 7: Updated plot of correlation analysis

Figure 8 (concept of rotating cylinder): dropped

Tables

We updated Table 1 by dropping those lines referring to events which we could not analyse anymore with the new method. We dropped the columns “DoY”, “K” and “Angular BV Frequency”.

We thank Referee #2 for his valuable comments.

Passages in red have been deleted or rephrased as indicated.

His general comments were:

1. “I have some concerns about the concept of Prölss (see also the specific comments at the end). The idea is that the mixing occurs at time scales of half a rotation of the cylinder. This time directly affects the derived eddy diffusion coefficient. However, the rotation will not be over after half a rotation but will continue and the vortex will disintegrate into smaller vortices etc. It may well be that the assumption that the mixing occurs at time scales of half a rotation leads to a systematic underestimation of the effective mixing time and hence to an overestimation of the eddy diffusion coefficients. This may also explain why your values of K are systematically larger than the literature values cited.”

We agree about the concerns Referee #2 has about the cylindrical concept of Prölss. Demanding a perfect rotating cylinder is a very strong assumption that may apply to some of the turbulent vortices but definitely not to all of them. We decided to follow his advice and adapted the method of Hecht et al. (2021) following Chau et al. (2020). We refrained from determining K from a rotating cylinder model. Instead, we read the feature size L and the residual velocity v_{res} from the image series and directly calculated ε by using the equation $\varepsilon = C \frac{v_{res}^3}{L}$ with $C \approx 1$ (Hecht et al., 2021). As Referee #1 assumed correctly, this was not always easy for all our examples. Staying with the episodes where the derivation of ε was possible with this method, our data basis reduced from 45 to 25 episodes. This changed the results of our correlation analysis with gravity wave activity: We now hardly see any significant correlation with the activity of gravity waves between 6 and 480 min.

Although the values are now a bit lower (the rotating cylinder model certainly served as an upper boundary value since it assumed maximum mixing; Referee #2 stated this quite correctly) some of them still exceed the limit of 1 W/kg with the maximum being 9 W/kg. We provide a careful discussion of the deviations from previous studies.

As the derivation of ε is quite difficult and due to the variety of turbulent episodes we furthermore decided to show more of our turbulent observations. Besides our former video supplement from 4 November 2018, we now present three more video sequences.

2. “Please show a sample 2-D FFT spectrum.”

As Referee #2 desired, we now show a sample 2-D FFT in Figure 1. We also present the respective image, where the wave structure can be recognized.

Referring to his specific comments:

Line 37: We changed “ground” to “troposphere”.

Line 68: We changed “These” to “Remote sensing techniques”.

Line 74: We changed “Proceedings” to “Improvements”.

Line 104: “automatic measurements with focus on the OH* airglow”

“What does this mean (i.e. “with focus on”)? Has a filter been used to remove the O2 singlet delta emission?”

No, we have not used any filter. Our formulation “with focus on” refers to the OH* emissions dominating the spectral range between 0.9 and 1.7 μm where our camera system integrates. The influence of O2 singlet delta has been studied by Hannawald et al (2016), who found no significant influence of O2 singlet delta in the FAIM data as long as short-term fluctuations (in the gravity wave period range) well after evening twilight are studied (see Figures 6 and 7 in Hannawald et al. (2016)).

Lines 14, 38, 49, 55, 72, 77, 108, 186, 264, 269, 272, 279, and 312: We put commas before and behind “e.g.”.

Line 124: “Due to the small FOV of FAIM 3 we renounce the application of a star removal algorithm”

“Please comment briefly on the effect of stars on the results.”

Although being rather bright, stars are quite small and have sizes of just a few pixels. Removing them has not altered the spectra in those ranges that were of interest for us, so we refrained from removing them to save computational power and avoid pixel interpolation in the images.

Line 128: “A fitted linear intensity gradient - This fitting is done before the FFT, right?”

Yes, the subtraction of the linear intensity gradient is done before the FFT. We clarified this by adding “...is subtracted from the input images...is applied during the 2d-FFT...”.

Line 136: “Wave structures with horizontal wavelengths of half the FOV size still showed a strong bias toward phases 0 or pi”

“Is there a simple reason for this behavior for long wavelengths?”

This behavior is caused by the application of a window function to the image prior to calculating the FFT (a Hann window in our case). The image mean is already subtracted so that wave maxima and minima will be represented by positive and negative values, respectively. The window function will fade the values towards the image borders to zero. If a wave maximum of a pretty large wave is showing only one maximum in the middle of the FOV, the window function will not damp its intensity because the maximum is far away from the image borders. One maximum (in the image center) and two minima (towards the image borders) will be seen in the image. If the phase shifts so that one maximum at each border of the image and one minimum in the image center are visible, the maxima will be damped towards zero by the windowing. What remains is a much lower intensity wave which might be overseen in the spectrum due to its underestimated amplitude. So in conclusion, for large waves (regarding the FOV size), the phase matters

when identifying these waves. Not applying a specific window function (i.e. applying a rectangular window with hard edges at the image borders) is no solution either, as the “sidelobes” of the actual wave signals will have a large effect which would lead to additional pseudo-wave signals in the spectrum with amplitudes almost comparable with the actual wave signal. Our tests showed that all remnants of this effect disappeared for wavelengths below half of the FOV size.

Line 166: “Ca. 63 % of the observed wave events have periods longer than the respective BV period and will be referred to as gravity wave events in the following.”

“What about the remaining signatures? What are they? Probably Doppler-shifted GWs?”

Yes, probably Doppler-shifting plays an important role here. As also Referee #1 claimed, setting the BV period as a limit for gravity waves is problematic without having accurate wind data. This is why we refrained from distinguishing between waves above and below the BV period and analysed the wave-like structures as they are. We assume that they are related to instability features like ripples.

We inserted the passage “Please note that we are using the word ‘wave’ for all wave-like structures we find in the images. The question whether these are actual gravity waves is discussed in section 5.” at the beginning of section 4.1 to clarify the more convenient usage of the word ‘wave’ instead of ‘wave-like structures’ while presenting the results.

Line 168: “here you distinguish between waves and gravity waves. See my previous comment.”

See our previous answer.

Line 184: Referee #2 stated: “Unless the rotational axis is aligned perpendicular to the image plane, the three-dimensional vortex rotation manifests as more than one coherent structure that is moving against or overtaking each other. I read this sentence several times, but didn’t really understand it. The grammar (singular/plural) is also not fully correct (“that is moving against or overtaking each other”).”

As this sentence belongs to the cylindrical mode, we deleted it entirely.

Line 207: Yes, we were aware of this geometric effect and always read the fastest velocity of each patch to make sure that we did not read its velocity while it was located on a cylinder side.

Line 239: We added the missing degree sign behind “6.2”.

Page 8, last paragraph: “If understood correctly, then completely different spatial scales are compared here, right? Several hundred km (spectrometer) vs. a few km (FAIM). Perhaps this can/should be mentioned explicitly.”

Yes, it is a good idea to mention this explicitly. We added “Note that the spectrometer GRIPS is sensitive to much larger spatial scales than FAIM.” in Line 417.

Line 252: “The directions of propagation are quite uniformly distributed over all quadrants as can be seen in Figure 2.”

“Well, looking at the figure, I disagree.”

We changed the formulation to “As can be seen in Figure 3, the wave structures we observed exhibit multiple directions.”

Line 293: We corrected “In principal” to “In principle”.

Line 309: “The here-presented values of K exhibit a magnitude of $10^3 - 10^4 \text{ m}^2\text{s}^{-1}$, which partly agrees with recent results, although some of our values are higher.”

“Your values are 2 orders of magnitude larger than the ones published by Lübken. This is quite a large difference. The Liu values are an order of magnitude smaller. Potential reasons should be discussed.

Regarding the Prölss-concept to derive K : I’m not sure, whether this concept applicable to measurements capturing the rotating structures at different stages of the evolution of the structures? The cascade will go from a large eddy to many smaller eddies and I’m not sure what effect it makes, if the structure is analyzed at different times?”

See our changes in this major comment above.

Line 330: “Given that our analyzed episodes are typical representatives of turbulent wave breaking, dynamical heating by gravity wave dissipation would deliver the same effect within few minutes as does chemical heating during an entire day.”

“One should keep in mind that the chemical heating is quasi-global and not intermittent in space and time, whereas the dynamical heating is probably quite local. The heating rates only apply to the air volumes affected by the turbulent motion. It would be interesting to estimate what fraction of the global MLT region experiences events (and how many) on a given day.”

Yes, we are well aware of the fact that our dynamical heating rates are strongly localized and intermittent, while the chemical heating rates by Marsh are global and referring to the whole day.

We made this clearer to the reader by changing the formulation to “within few minutes at very localized areas in the UMLT as does chemical heating during an entire day for the whole atmosphere.”

We agree that it would be quite interesting to rescale the intermittent and localized dynamical heating contributions to a global and continuous reference. Certainly, more than just 25 measurements within one and a half years would be needed to do this properly. We believe that setting up more FAIM3-like systems at various sites will be the key for that.

Line 393: “We find an isotropic distribution of directions of propagation”

“Looking at the figures, it is not really isotropic, is it?”

We weakened this statement to “We generally find variable directions of propagation”.

Line 347: “and agree mostly with earlier results from rocket and lidar measurements and simulations.”

“I disagree. The Lübken values are 2 orders of magnitude smaller (rocket) and the cited lidar values one order of magnitude. Please revise this statement.”

We of course revised this statement and changed it to “and are higher than earlier rocket measurements.”

Appendix A: “I checked the derivation and it seems to be OK. But I have one general question: The model assumes that the mixing occurs on time scales of one half rotation. However, the rotation will go on and after one full cycle the original state is reached again (assuming a rigid cylinder). And this will go on several more cycles until the vortex disintegrates to smaller vortices. In reality this is of course much more difficult, but I think the model may underestimate the effective mixing time and hence overestimate the turbulent diffusion coefficient. Perhaps this is the reason why your estimates are larger than the other ones?”

We agree to this assumption, see our answer to the major comments above.

„And a minor comment on the appendix: The term “side gas” is quite unusual and I don’t know what it means to be honest. Is this a problem with the translation from German? I suggest to use another term.“

In the course of our changes from the cylindrical model to the approach of Hecht et al. (2021), we dropped the entire appendix.

Changes made in the manuscript:

Abstract

Lines 14, 38, 49, 55, 72, 77, 108, 186, 264, 269, 272, 279, and 312: We put commas before and behind “e.g.”.

Line 16f: Added “instability features from breaking secondary waves”

Line 17: Replaced “originating from breaking primary waves” by “that were created” and dropped “(westward)” and “(summer)”.

Line 20f: We changed “Furthermore, observations of turbulent vortices allowed the estimation of eddy diffusion coefficients in the UMLT from image sequences in 45 cases. Values range around $10^3 - 10^4 \text{ m}^2\text{s}^{-1}$ and mostly agree with literature. Turbulently dissipated energy is derived taking into account values of the Brunt-Väisälä frequency based on TIMED-SABER (Thermosphere Ionosphere Mesosphere Energetics Dynamics, Sounding of the Atmosphere using Broadband Emission Radiometry) measurements as presented by Wüst et al. (2020). Energy dissipation rates range between 0.63 W kg^{-1} and 14.21 W kg^{-1} leading to an approximated maximum heating of 0.2-6.3 K per turbulence event. These are in the same range as the daily chemical heating rates reported by Marsh (2011), which apparently stresses the importance of dynamical energy conversion in the UMLT.”

to

“We present multiple observations of turbulence episodes captured by our high-resolution airglow imager and estimated the energy dissipation rate in the UMLT from image sequences in 25 cases. Values range around 0.08 and 9.03 W kg^{-1} and are higher than those in recent literature. The values found here would lead to an approximated localized maximum heating of 0.03-3.02 K per turbulence event. These are in the same range as the daily chemical heating rates for the entire atmosphere reported by Marsh (2011), which apparently stresses the importance of dynamical energy conversion in the UMLT.”

Introduction

Line 40: We changed “ground” to “troposphere”

Lines 54ff: We changed

“They cause turbulent mixing of the medium, which is described by the eddy diffusion coefficient K . K can be calculated from the eddy radius r_e and the circumferential velocity v_e by

$$K = \frac{2}{3\pi} r_e v_e \quad (1)$$

(see e.g. Prölss, 2001. The derivation is outlined in detail in appendix A.). According to Weinstock (1978), knowing K and the BV frequency N , an estimate for the energy dissipation rate ϵ - the rate at which turbulent kinetic energy is dissipated into heat at the short-scale end of the energy cascade of the inertial subrange (Li et al., 2016) - can be calculated using

$$K \approx 0.81 \cdot \left(\frac{\epsilon}{N^2}\right). \quad (2)$$

to

“They cause turbulent mixing of the medium, resulting in the dissipation of turbulent energy at an energy dissipation rate ϵ . According to the theory of stratified turbulence, ϵ depends on the characteristic length scale L and velocity scale U of the turbulent features. The energy dissipation rate is then given by

$$\epsilon = C_\epsilon \frac{U^3}{L} \quad (1)$$

(see, e.g., Chau et al, 2020; who apply this equation to radar observations of KHs). C_ϵ is a constant which is found to be equal to 1 (Gargett, 1999).”

Lines 70ff: We changed

“This is why turbulence investigations in the UMLT are challenging and there are only few values of K available at UMLT heights. Lübken et al. (1997) use rocket measurements to retrieve K and ϵ in the height range 65-120 km. Liu (2009) presents a method for the estimation of K from gravity wave momentum fluxes derived from lidar data. Baumgarten & Fritts (2014) use imaging techniques of mesospheric noctilucent clouds to investigate the formation of KHs and the onset of turbulence.”

to

“This is why turbulence investigations in the UMLT are challenging and there are only few values of ϵ available at UMLT heights. Lübken et al. (1997) use rocket measurements to retrieve ϵ in the height range 65-120 km. Baumgarten & Fritts (2014) use imaging techniques of mesospheric noctilucent clouds to investigate the formation of KHs and the onset of turbulence.”.

Line 76: We changed “These include...” to “Remote sensing techniques include...”

Line 83: We changed “Proceedings” to “Improvements”

Data Basis

Line 138: We inserted “...from the input images...” during the 2d-FFT”.

Line 156: We inserted “An exemplary event and the respective 2-dimensional spectrum are shown in Figure 1. We often observe episodes of turbulence in our image series that exhibit the typical dynamics of vortex formation and quasi-chaotic behavior.”

Line 164: Replaced “45” by “25” and “vortex” by “turbulence”

Lines 166ff: Omitted “For both, gravity wave statistics (section 4.1) and the calculation of the energy dissipation rate (section 4.2) the BV frequency is required, which is adapted from the climatology presented by Wüst et al. (2020). It is based on TIMED-SABER (Thermosphere Ionosphere Mesosphere Energetics Dynamics, Sounding of the Atmosphere using Broadband Emission Radiometry) temperature data and takes into account the seasonal variability of the angular BV frequency. The climatology of the grid point (45° N, 10° E) is used, which is closest to our FOV. Depending on the day of the year (DoY) the BV frequency is given by

$$N = 2.20 \cdot 10^{-2} \text{s}^{-2} + 0.19 \cdot 10^{-2} \text{s}^{-2} \sin\left(\frac{2\pi}{324.51 \text{d}} \cdot \text{DoY} - 2.02\right) + 0.05 \cdot 10^{-2} \text{s}^{-2} \sin\left(\frac{2\pi}{180.00 \text{d}} \cdot \text{DoY} + 1.61\right). \quad (3)$$

We use an uncertainty of $\pm 5\%$ as according to Wüst et al. (2020) 91% of their data lie within this range around the harmonic approximation. The BV period is then referred to as $\tau_{BV} = \frac{2\pi}{N}$.

Results

We inserted the passage “Please note that we are using the word ‘wave’ for all wave-like structures we find in the images. The question whether these are actual gravity waves is discussed in section 5.” at the beginning of section 4.1.

Line 165 ff: We dropped “For each wave event the individual BV period is calculated based on Eq. (3) and the DoY. Ca. 63% of the observed wave events have a period longer than the respective BV period and will be referred to as gravity wave events in the following. Their statistical contribution is highlighted in grey in Fehler! Verweisquelle konnte nicht gefunden werden..”

Line 168 f: We dropped “The median value of gravity wave periods is found at 517 s (8.6 min).”.

Line 169: 17.6 m/s changed to 139.8 m/s; 7.9 m/s changed to 13.3 m/s

Line 170: 3.3 m/s changed to 10.3 m/s. 50.7 % (49.3 %) changed to 52.7 % (47.3 %). Dropped the word “gravity”.

Line 171: Dropped the word “gravity”.

Line 172: 5.4 m/s (5.3 m/s) changed to 9.4 m/s (8.2 m/s). 3.0 m/s (3.1 m/s) changed to 8.9 m/s (7.4 m/s).

Line 173: 53.8 % changed to 56.0 %. 46.2 % changed to 44.0 %.

Line 174: 47.9 % changed to 49.5 %.

Line 175: 52.1 % changed to 50.5 %. 44.4 % (53.5 %) changed to 42.0 % (55.7 %).

Line 176: 4.7 m/s (5.3 m/s) changed to 7.5 m/s (9.4 m/s).

Line 177: 3.0 m/s (3.2 m/s) changed to 7.1 m/s (8.7 m/s).

Lines 192 ff: We added: “To give an impression of the turbulent dynamics we observe, we present four of our turbulence episodes as video supplement. On 16 November 2017, 02:16 UTC, the turbulent breakdown of parts of an extended wave field can be observed (video 1). On 6 December 2017, 00:26 UTC, several fronts seem to be building up and form rotating vortices (video 2). This can be observed even clearer on 14 October 2018, 17:08 UTC, where the residual movement of turbulent features can be well recognized above the general background movement (video 3). On 4 November 2018, 19:18 UTC, breaking wave fronts seem to form rotating structures of nearly cylindrical shape, while these are accompanied by other turbulently moving eddies (video 4).

We estimate the turbulent energy dissipation rate ϵ using equation (1). However, in contrast to Chau et al. (2020) who used radar measurements, we only have horizontal information from our airglow imager. Hecht et al. (2021) demonstrate an approach how to apply equation (1) to purely horizontal airglow imager data, which we adapt to our observations in the following. The characteristic length scale L can be read from the images by measuring the size of the turbulent features. The velocity scale is given by the residual velocity v_{res} of these features. In our observations, they are part of

larger instability features, which we assume to be advected by the background wind. We determine v_{res} by reading the actual velocity of the turbulent features and subtracting the background movement v_{bg} in the resulting direction. This is exemplarily shown in Figure 4. The two patches highlighted therein are both moving to the upper right direction but are approaching each other. This helps distinguishing background and residual movement.”

and dropped:

“The eddy parameters needed for the calculation of the eddy diffusion coefficient (Eq. 1) are determined manually from the image series of the 45 observations of turbulence. It has to be kept in mind that we are deriving properties of a three-dimensional movement from two-dimensional data.

We assume the vortices to rotate in a perfect circular shape. The lateral expansion creates the impression of a rotating cylinder. Coherently moving structures give indication of the horizontal velocity vector. Unless the rotational axis is aligned perpendicular to the image plane, the three-dimensional vortex rotation manifests as more than one coherent structure that is moving against or overtaking each other (see e.g. Sedlak et al., 2016; Figure 6 therein). During data inspection we noticed that the orientation of the rotational axis can be aligned in any direction. It tends to be parallel to the image plane when it evolves directly from the crests of a breaking wave. However, we could also observe eddies rotating around an axis aligned almost perpendicular to the image plane. An example of a rotating vortex within a FAIM 3 snapshot on 4 November 2018 at 19:36:41 UTC is displayed in Figure 3a. The rotational axis and the direction of rotation are marked therein and on an actual cylinder (Figure 3b) for clarification. Since it is very difficult to identify a vortex structure in a single picture we have attached a video sequence of this episode (Video 1). The vortex radius and velocity are read from the images. Besides measuring the vortex rotation, it has also to be taken care of the overall image: if additional to the eddy movement all structures in the FOV are moving into a common direction, this background motion has to be subtracted. In the example shown above the vortex is advected toward the left corner. The distance between camera and observed vortex is much larger than the expansion of the vortex along the rotation axis so that falsifications arising from different perspectives of the vortices can be neglected. This principle is illustrated in Figure 4. As the vortices are three-dimensional the alignment of the rotational axis should not affect the value of the vortex parameters in the images: it does not matter if the axis is aligned perpendicular, parallel or in any other angle to the image plane, the vortex size will be accessible from the two-dimensional projection of the image assuming circular eddy movement. The same holds for the circumferential velocity since both the radius and the circulation time remain unchanged. However, perfectly circular eddy rotation does not necessarily occur in nature. Deviations from circularity can lead to both over- and underestimation of vortex sizes depending on the vortex orientation. Since isotropy is one of the characteristic properties of turbulent movements one may presume that from a statistical point of view both cases occur equally so that no systematic error is made.”

Lines 232ff: We changed

“As stated in section 3 we found 45 episodes of turbulence that allowed the derivation of the vortex radius and circumferential velocity. The resulting eddy diffusion coefficients K are shown in **Fehler! Verweisquelle konnte nicht gefunden werden.** We assume a general read-out error of ± 3 pixels, which corresponds to a distance of ± 72 m. The circumferential velocity is determined by reading the distance a patch on the rotating cylinder surface covers within an episode of at least ten images, which corresponds to a time span of 28 s. Thus, the circumferential velocity is estimated with an

error of $\pm 2.6 \text{ ms}^{-1}$. The arising uncertainties of K are calculated following the rules of error propagation.

The values of K range from 0.12 to $1.94 \cdot 10^4 \text{ m}^2\text{s}^{-1}$. The mean value is $0.76 \cdot 10^4 \text{ m}^2\text{s}^{-1}$

to

“As stated in section 3 we found 25 episodes of turbulence that allowed the derivation of L and v_{res} . Using equation (1), the energy dissipation rate is then calculated by $\epsilon = \frac{v_{res}^3}{L}$. The resulting values are shown in **Fehler! Verweisquelle konnte nicht gefunden werden.** We assume a general read-out error of ± 3 pixels, which corresponds to a distance of $\pm 72 \text{ m}$. Velocities are determined by reading the distance a feature covers within an episode of at least ten images, which corresponds to a time span of 28 s. Thus, velocities are estimated with an error of $\pm 2.6 \text{ ms}^{-1}$. The arising uncertainties of ϵ are calculated following the rules of error propagation.

The values of ϵ range from 0.08 to 9.03 W kg^{-1} . The median value is 1.45 W kg^{-1} ”

Lines 240ff: We dropped

“(standard deviation of $0.53 \cdot 10^4 \text{ m}^2\text{s}^{-1}$) and we retrieve a median of $0.59 \cdot 10^4 \text{ m}^2\text{s}^{-1}$. It is difficult to exactly quantify the error of manual parameter determination from the images. However, in this work we rather focus on the order of magnitude of K . When calculating K two distance values are read from the images (one for the vortex size and one for the determination of the circumferential speed). Considering Eq. (1), a mistake of factor 10 is made for K if these distances are misread by a factor of at least $\sqrt{10}$. The shortest (and therefore most difficult to determine) diameter in our analysed examples was 768 m. For an error of one order of magnitude of K this distance must be misread as either shorter than 243 m or longer than 2428 m, i.e. a distance of 32 pixels must be wrongly interpreted as shorter than 9 pixels or longer than 101 pixels. This lies far beyond the read-out uncertainty of ± 3 pixels we introduced above and can be assumed to be much worse than any read-out error one would normally make.

The energy dissipation rate ϵ can be estimated from the eddy diffusion coefficient K according to Eq. (2) using the BV frequency as described by Eq. (3).

As can be seen in **Fehler! Verweisquelle konnte nicht gefunden werden.** the energy dissipation rate of the observed turbulence events is in the range $0.63 - 14.21 \text{ W kg}^{-1}$.”

Line 254: We updated “146 s” to “241 s” and “2.4” to “4.0”.

Line 258: We updated “220” to “30” and “6346” to “3015”.

Line 262: We updated “0.2-6.3 K” to “0.03-3.02 K” and dropped “64% (21 out of 33) of these values are larger than one Kelvin.”

Line 268: We inserted a missing “”

Lines 277ff: We changed “We find a slight but significant anticorrelation for gravity wave periods in the range 122-207 min. For these periods the mean value of the correlation coefficient is -0.46. The highest coefficient of anticorrelation is -0.52 at a period of 178 min. ”

to

“We find almost no significant correlation for any gravity wave period.”

Discussion:

Line 280: We replaced “The directions of propagation are quite uniformly distributed over all quadrants as can be seen in Figure 2” by “As can be seen in Figure 3, the wave structures we observed exhibit multiple directions.”

Line 288: We replaced “(positive zonal phase speed) and in westward direction during summer. Although this tendency is quite weak,” by “whereas zonal directions are quite balanced during summer. Although the eastward tendency during winter is quite weak,”.

Line 290: We added “tropospheric and”.

Lines 292ff: We replaced “The reversed stratospheric winds during summer would consequently allow some more eastward travelling gravity waves to propagate upward (see e.g. Hoffmann et al., 2010; Hannawald et al., 2019). Since the highest observed phase speed of waves with periods longer than the BV period is only 17.6 m s⁻¹, it can be assumed that in the majority we do not observe gravity waves that are originating from low altitudes and are fast enough not to be blocked by the stratospheric wind fields.”

by

“During summer the stratospheric winds reverse to westward direction, so that eastward oriented gravity waves are filtered in the tropopause and westward oriented gravity waves are filtered in the stratosphere (see, e.g., Hoffmann et al., 2010; Hannawald et al., 2019).”.

We inserted

“As we have no accompanying wind measurements in the height of our observations it is difficult to decide by means of the period whether the wave structures presented in section 4.1 are small-scale gravity waves or instability features. Ca. 63 % of the observed wave events have an observed period above the BV period (here we used the climatology presented by Wüst et al., 2020), however these could also be Doppler-shifted instability features instead of gravity waves. While the distinction between largely extended wave-fields (bands) and small localized wave structures that are related to instability (ripples) is often made at a horizontal wavelength of 10 - 20 km (Taylor et al., 1997; Nakamura et al., 1999), Li et al. (2017) remark that even structures with horizontal wavelengths of 5 - 10 km may sometimes be gravity waves rather than instability features.”

after this passage.

Line 302 ff: We changed “Considering the directional distribution, it is possible that the major part of our waves may” to “If this would be true for our small-scale wave structures, they might rather”.

Line 321 f: We changed “southward in 62 % of cases.” to “southward in 71 % of cases.”.

We inserted

“However, regarding the small horizontal wavelengths below 4.5 km, it is more likely that the major part of the observations presented in section 4.1 are related to instability features. The quite slow phase speeds (mean value 13.3 m / s) are one hint for this as typical gravity wave phase speeds accumulate around 40 m / s (see, e.g., Wachter et al., 2015 and Wüst et al., 2018). If Figure 3b was the phase speed distribution of gravity waves, it is likely that a majority of them would encounter critical levels somewhere and would not be observable in the OH* layer.”

after this passage.

Line 371 ff: We replaced “Li et al. (2017) report that ripples are hard to distinguish from small-scale gravity waves. Height-resolved measurements of the horizontal wind would be needed to determine the local wind shear and make a profound statement about atmospheric instability. Nevertheless,”

by

“Considering the fact that the directional peculiarities of our observed wave events fit well with the expected behavior of secondary gravity waves, as discussed above, support the scenario of the wave structures being ripples from dynamic instabilities of secondary gravity waves, that originate from the stratospheric and mesospheric jet.”

We added

“Nevertheless, height-resolved measurements of the horizontal wind would be needed to determine the local wind shear and make a profound statement about atmospheric instability. It has to be kept in mind that a 2d-FFT was used. Thus, periodic structures are assumed to be stationary, i.e., they extend over the entire image. Faint structures that appear only in small parts of the image (as does for example the 550m wave packet in Sedlak et al., 2016; Fig. 2) would be underrepresented by this analysis.”

at the end of the discussion section of the wave statistics.

Lines 384ff:

We changed

“There are still very few measurements of turbulent eddy diffusion coefficients in the UMLT. Lübken (1997) reports K to be around $10^1 - 10^2 \text{ m}^2\text{s}^{-1}$ at a height of 87 km at high latitudes. Hodges (1969) states that the eddy diffusion coefficient caused by gravity waves is typically around $10^3 \text{ m}^2\text{s}^{-1}$. According to the CIRA (Committee on Space Research (COSPAR) International Reference Atmosphere) climatology of 1986 (NASA National Space Science Data Center, 2007) global values range between magnitudes of 10^2 and $10^3 \text{ m}^2\text{s}^{-1}$. LIDAR measurements above New Mexico, USA deliver values that vary strongly around a magnitude of $10^2 \text{ m}^2\text{s}^{-1}$ (Liu, 2009). Smith (2012) notes that the WACCM (Whole Atmosphere Community Climate Model) climatology exhibits rather small values with magnitude $10^1 \text{ m}^2\text{s}^{-1}$ and that the huge discrepancies of K estimates cannot be fully explained yet. The here-presented values of K exhibit a magnitude of $10^3 - 10^4 \text{ m}^2\text{s}^{-1}$, which partly agrees with recent results, although some of our values are higher.”

to

“Measuring the eddy diffusion coefficient in the UMLT is still challenging and there are only few studies yet. Rocket measurements of Lübken (1997) deliver energy dissipation rates between ca. 0.01 and 0.1 W kg⁻¹ between 85 and 90 km height at high latitudes. Chau et al. (2020) find an energy dissipation rate of 1.125 W kg⁻¹ for their KHI event observed in the summer mesopause and state that this a rather high value compared to the findings of Lübken et al. (2002). Hocking (1999) provides a rescaled overview of earlier values of the energy dissipation rate and these have a maximum magnitude of 0.1 W kg⁻¹. Hecht et al. (2021) derive a value of 0.97 W kg⁻¹ from airglow images of a KHI event. Ranging from 0.08 up to 9.03 W kg⁻¹ the values of energy dissipation rate derived here are higher than reported by other studies. However, the median value of 1.45 W kg⁻¹ is not too far away from the values of Chau et al. (2020) and Hecht et al. (2021).”.

Lines 402f: We added “– except for the studies of Hecht et al. (2021), whose value is quite similar to the median value of our data –,”

Lines 405ff: We dropped “Nevertheless, the agreement of the above-mentioned authors on eddy parameters in the UMLT is quite good, considering the fact that energy dissipation rate in the upper troposphere and lower stratosphere varies by a factor of more than five orders of magnitude (Li et al., 2016).”.

Line 408: Changed “vortex” to “turbulence”

Line 409: Changed “Circumferential speed and vortex radius” to “The length scale and velocity scale of turbulent features”

Line 410: “and we” changed to “. We”

Lines 412f: Inserted “However, using equation (1) velocity dominates the length scale due to its power of 3, so that ϵ strongly depends on a parameter, which is quite difficult to extract from the images.”

Line 414: Dropped “eddy diffusion coefficient and”

Line 415: Replaced “eddy diffusion coefficients” by “energy dissipation rate” and replaced “significant anticorrelation” by “no significant correlation”

Lines 416: Changed “122-207 min” to “6-480 min”

Lines 416ff: Changed

“One may assume that turbulent vortices we observe could be predominantly attributed to breaking gravity waves in this period range. If this was the case, stronger wave breaking would manifest as higher eddy diffusion coefficients and result in a lower activity of gravity waves with periods 122-207 min in the UMLT. However, especially observations of period-resolved gravity wave activity at altitudes below would be needed to confirm this assumption.

Assuming that the turbulently dissipated energy is entirely converted into heat we find temperature changes of 0.2-6.3 K that occur within time spans of 2.4-15.4 min. Marsh (2011) report chemical heating rates in the atmosphere to be around 3-4 K per day. Given that our analysed episodes are typical representatives of turbulent wave breaking, dynamical heating by gravity wave dissipation would deliver the same effect within few minutes as does chemical heating during an entire day.”

to

“Turbulence thus cannot be related to distinct periods of the gravity wave spectrum with the here-presented data. Note that the spectrometer GRIPS is sensitive to much larger spatial scales than FAIM. A larger data basis of turbulence parameters and especially observations of period-resolved gravity wave activity at altitudes below will be needed to answer the question if all parts of the gravity wave spectrum drive turbulence generation in the UMLT equally.

Assuming that the turbulently dissipated energy is entirely converted into heat we find temperature changes of 0.03–3.02 K that occur within time spans of 4.0–15.4 min. Marsh (2011) report chemical heating rates in the atmosphere to be around 3–4 K per day. Given that our analysed episodes are typical representatives of turbulent wave breaking, dynamical heating by gravity wave dissipation would deliver the same effect within few minutes at very localized areas in the UMLT as does chemical heating during an entire day for the whole atmosphere.”

Summary

Lines 429ff: We changed

“We present an analysis of small-scale wave dynamics from OH* imager data acquired between 26 October 2017 and 6 June 2019 at Otlica Observatory, Slovenia. Measurements have been performed with the imager FAIM 3, which has a spatial resolution of ca. 24 m pixel⁻¹ and a temporal resolution of 2.8 s.

Wave structures in the images are systematically identified by applying a 2d-FFT to nocturnal image sequences during clear sky episodes. All wave events meeting our persistency criteria were used to derive a statistical analysis of wave structures with horizontal wavelengths between 48 m and 4.5 km. 63% of the wave events have a period longer than the BV period and may be tentatively considered as gravity waves. We find an isotropic distribution of directions of propagation, which indicates that wave structures may be mostly created above the stratospheric wind fields. However, a weak seasonal dependency is found: zonal directions of wave propagation are slightly more eastward during winter and westward during summer. We speculate these to be generated by breaking gravity waves in the course of wind filtering, receiving their zonal direction through advection by the background wind. We find a stronger tendency of southward propagation during summer, which may point to a vital role of gravity wave filtering and excitation of secondary waves by the meridional mesospheric circulation. It is possible that secondary waves and instability features represent the majority of our observed waves.

Furthermore, we estimated turbulence parameters from 45 episodes of vortex observations. The derived values of eddy diffusion coefficients are in the range around $10^3 - 10^4 \text{ m}^2\text{s}^{-1}$ and agree mostly with earlier results from rocket and lidar measurements and simulations. Considering the respective values of the BV frequency as calculated by Wüst et al. (2020) we retrieve energy dissipation rates between 0.63 W kg^{-1} and 14.21 W kg^{-1} , that cause estimated heatings by 0.2–6.3 K per turbulence event. These have the same order of magnitude”

to

“We present an analysis of small-scale dynamics of instability features and turbulence from OH* imager data acquired between 26 October 2017 and 6 June 2019 at Otlica Observatory, Slovenia.

Measurements have been performed with the imager FAIM 3, which has a spatial resolution of ca. 24 m pixel⁻¹ and a temporal resolution of 2.8 s.

Wave-like structures in the images are systematically identified by applying a 2d-FFT to nocturnal image sequences during clear sky episodes. All events meeting our persistency criteria were used to derive a statistical analysis of wave-like structures with horizontal wavelengths between 48 m and 4.5 km. The small horizontal scales are a strong hint that these are likely instability features of breaking gravity waves like ripples. We generally find variable directions of propagation, which indicates that these wave-like structures may be mostly created above the stratospheric wind fields. However, a weak seasonal dependency is found: zonal directions of propagation are slightly more eastward during winter and westward during summer. We speculate these to be instability features generated by breaking secondary gravity waves, receiving their zonal direction through advection by the background wind. We find a stronger tendency of southward propagation during summer, which may point to a vital role of gravity wave filtering and excitation of secondary waves and their subsequent instability features by the meridional mesospheric circulation.

Furthermore, we observed and presented OH* imager observations of turbulence with high spatio-temporal resolution. We estimated turbulence parameters from 25 episodes of eddy observations. Following the approach of Hecht et al. (2021) we derived the energy dissipation rates for our observed events by reading the turbulent length and velocity scale from the image series. Our values range between 0.08 and 9.03 W kg⁻¹ and are higher than earlier rocket measurements. The values presented here would cause localized heatings of 0.03-3.02 K per turbulence event. The largest of these reach the same order of magnitude”

Appendix

We dropped Appendix A.

Figures

Figure 1 is now a sample event with its 2D-FFT spectrum.

Figure 2 (former Figure 1): Histograms of wave parameters without separation by the BV period

Figure 3 is now former Figure 2

Figure 4 (former Figure 3): New snapshot showing how to read the new wave parameters from the images.

Former Figure 4: dropped

Figure 5: Plot of temporal course and histogram of ϵ (no K values anymore)

Figure 6: Updated histogram of temperature changes

Figure 7: Updated plot of correlation analysis

Figure 8 (concept of rotating cylinder): dropped

Tables

We updated Table 1 by dropping those lines referring to events which we could not analyse anymore with the new method. We dropped the columns “DoY”, “K” and “Angular BV Frequency”.

Gravity wave instability structures and turbulence from more than one and a half years of OH* airglow imager observations in Slovenia

René Sedlak¹, Patrick Hannawald^{1,2}, Carsten Schmidt², Sabine Wüst², Michael Bittner^{1,2}, and Samo Stanič³

5 ¹Institute of Physics, University of Augsburg, Augsburg, Germany

²German Remote Sensing Data Center, German Aerospace Center, Oberpfaffenhofen, Germany

³Center for Astrophysics and Cosmology, University of Nova Gorica, Ajdovščina, Slovenia

Correspondence to: René Sedlak (rene.sedlak@physik.uni-augsburg.de)

Abstract. We analysed 286 nights of data from the OH* airglow imager FAIM 3 (Fast Airglow IMager) acquired at Otlica
10 Observatory (45.93°N, 13.91°E), Slovenia between 26 October 2017 and 6 June 2019. Measurements have been performed
with a spatial resolution of 24 m pixel⁻¹ and a temporal resolution of 2.8 s.

A two-dimensional Fast Fourier transform is applied to the image data to derive horizontal wavelengths between 48 m and
4.5 km in the upper mesosphere / lower thermosphere (UMLT) region. In contrast to the statistics of larger scale gravity waves
(horizontal wavelength up to ca. 50 km, e.g., Hannawald et al., 2019) we find a more isotropic distribution of directions of
15 propagation, pointing to the presence of wave structures created above the stratospheric wind fields. A weak seasonal tendency
of a majority of waves propagating eastward (~~westward~~) during winter (~~summer~~) may be due instability features from ~~to~~
breaking secondary gravity waves originating from breaking primary waves that were created in the stratosphere. We also
observe an increased southward propagation during summer, which we interpret as an enhanced contribution of secondary
gravity waves created as a consequence of primary wave filtering by the meridional mesospheric circulation.

20 We present multiple observations of turbulence episodes captured by our high-resolution airglow imager. Furthermore,
observations of turbulent vortices allowed the estimation and estimated of eddy diffusion coefficients the energy dissipation
rate in the UMLT from image sequences in 45–25 cases. Values range around 0.08 and 9.03 W kg⁻¹ 10³–10⁴ m²s⁻¹ and
mostly agree with are on average higher than those in recent literature. Turbulently dissipated energy is derived taking into
account values of the Brunt Väisälä frequency based on TIMED SABER (Thermosphere Ionosphere Mesosphere Energetics
25 Dynamics, Sounding of the Atmosphere using Broadband Emission Radiometry) measurements as presented by Wüst et al.
(2020). Energy dissipation rates range between 0.63 W kg⁻¹ and 14.21 W kg⁻¹ leading The values found here would lead to
an approximated localized maximum heating of 0.03–3.02 K 0.2–6.3 K per turbulence event. These are in the same range as
the daily chemical heating rates for the entire atmosphere reported by Marsh (2011), which apparently stresses the importance
of dynamical energy conversion in the UMLT.

30

1 Introduction

Fully understanding the contribution of gravity waves to atmospheric dynamics is still a major issue when establishing climate models. Due to the various sources and mechanisms of interactions the effects of gravity waves have to be represented in these models using advanced parameterizations (Lindzen, 1981; Holton, 1983; de la Cámara et al., 2016) to cover as many aspects as it is possible given the restricted model resolution. Gravity waves exist on a large span of time scales ranging from several hours down to the Brunt-Väisälä (BV) period, which corresponds to ca. 4-5 min in the upper mesosphere / lower thermosphere (UMLT) region (Wüst et al., 2017b) and represents the smallest possible period of gravity waves. They show diverse behaviour depending strongly on wave properties like their periodicity (Fritts & Alexander, 2003; Beldon & Mitchell, 2009; Hoffmann et al., 2010; Wüst et al., 2016; Sedlak et al., 2020), which makes it even harder to fully account for them by means of parameterization. Furthermore, gravity wave generation is not restricted to the ground-troposphere but can also take place at higher altitudes, such as secondary wave excitation due to breaking gravity waves (see, e.g., Holton & Alexander, 1999; Satomura & Sato, 1999; Vadas & Fritts, 2001; Becker & Vadas, 2018).

As Fritts & Alexander (2003) state, it is necessary to metrologically capture all parts of the gravity wave spectrum. This includes especially dynamics on short scales where gravity wave breaking is induced by the development of instabilities. One of the most prominent features in this context is the formation of Kelvin-Helmholtz instability (KHI), which occurs as a consequence of a dynamically instable atmosphere due to wind shear (Browning, 1971). Gravity wave instability can also be of convective nature when growing wave amplitudes lead to a superadiabatic lapse rate (Fritts & Alexander, 2003). In general, atmospheric instabilities like KHIs often manifest as so-called ripples – periodic structures with small spatial dimensions and short lifetimes (Peterson, 1979; Adams et al., 1988; Taylor & Hapgood, 1990; Li et al., 2017).

Gravity wave breaking and the conversion of the transported energy into heat takes place in the course of turbulence. Once a wave breaks and motion shifts from laminar to turbulent flow energy is cascaded to smaller and smaller structures until viscosity becomes dominant over inertia and energy is dissipated into the atmosphere by viscous damping (see, e.g., Lübken et al., 1987).

The process of turbulence manifests as formation of vortices, so-called eddies. They cause turbulent mixing of the medium, which is described by the eddy diffusion coefficient K resulting in the dissipation of turbulent energy at an energy dissipation rate ϵ . According to the theory of stratified turbulence, ϵ depends on the characteristic length scale L and velocity scale U of the turbulent features. The energy dissipation rate is then given by

$$\epsilon K = C_\epsilon \frac{2}{3\pi} \frac{U^3}{L} r_e v_e \quad (1)$$

(see, e.g., Chau et al, 2020; who apply this equation to radar observations of KHIs). C_ϵ is a constant which is found to be equal to 1 (Gargett, 1999). ~~K can be calculated from the eddy radius r_e and the circumferential velocity v_e by~~

$$K = \frac{2}{3\pi} r_e v_e \quad (1)$$

(see e.g. Pröls, 2001. The derivation is outlined in detail in appendix A.). According to Weinstock (1978), knowing K and the BV frequency N , an estimate for the energy dissipation rate ϵ —the rate at which turbulent kinetic energy is dissipated into heat at the short scale end of the energy cascade of the inertial subrange (Li et al., 2016)—can be calculated using

$$K \approx 0.81 \cdot \left(\frac{\epsilon}{N^2} \right). \quad (2)$$

Gravity wave dissipation predominantly occurs in the upper mesosphere / lower thermosphere (UMLT) region (Gardner et al., 2002). Hocking (1985) states that the turbulent regime at this altitude manifests on scales shorter than 1 km, which sets high requirements for measurement techniques at these heights. This is why turbulence investigations in the UMLT are challenging and there are only few values of ϵK available at UMLT heights. Lübken et al. (1997) use rocket measurements to retrieve K and ϵ in the height range 65 - 120 km. Liu (2009) presents a method for the estimation of K from gravity wave momentum fluxes derived from lidar data. Baumgarten & Fritts (2014) use imaging techniques of mesospheric noctilucent clouds to investigate the formation of KHIs and the onset of turbulence.

At the same height, remote sensing measurements of the OH* airglow are an established access to UMLT dynamics. The OH* airglow is a layer at an average altitude of ca. 86–87 km with a full width at half maximum (FWHM) of ca. 8 km (Baker & Stair, 1988; Liu & Shepherd, 2006; Wüst et al., 2017b). These Remote sensing techniques include spectroscopic measurements of strong emission lines and the analysis of temperature time series derived from these (Hines & Tarasick, 1987; Mulligan et al., 1995; Bittner et al., 2000; Reisin & Scheer, 2001; Espy & Stegman, 2002; Espy et al., 2003; French & Burns, 2004; Offermann, 2009; Schmidt et al., 2013, 2018, Wachter et al., 2015; Silber et al., 2016, Wüst et al., 2016, 2017a, 2018), but also two-dimensional imaging in the short-wave infrared (SWIR) range (see, e.g., Peterson & Kieffaber, 1973; Hecht et al., 1997; Taylor, 1997; Moreels et al., 2008; Li et al., 2011; Pautet et al., 2014; Hannawald et al., 2016, 2019; Sedlak et al., 2016; Wüst et al., 2019 and many more).

The technology of OH* imaging has undergone a rapid technical progress over the last few decades. Proceedings Improvements in sensor technology and optics have provided the possibility to observe the signatures of gravity waves that manifest as periodic brightness variations in infrared images of the OH* airglow layer. The observations range from all-sky imaging of large-scale gravity waves (e.g., Taylor et al., 1997; Smith et al., 2009) to high resolution images of smaller gravity waves (Nakamura et al., 1999) and their breaking processes (Hecht et al., 2014; Hannawald et al., 2016). Hannawald et al. (2016) use an airglow imager called FAIM (Fast Airglow IMager) that is well-suited for the observation of small-scale gravity waves with a high temporal resolution of 0.5 s. Based on three years of continuous night-time observations at two different Alpine locations Hannawald et al. (2019) show statistics of gravity wave propagation for waves with horizontal wavelengths smaller than 50 km based on data of the same kind of instrument.

In 2016 we put into operation another FAIM instrument (FAIM 3) which still has a high temporal resolution of 2.8 s, but also a high spatial resolution of up to 17 m pixel⁻¹ (measurements in zenith direction utilizing a 100 mm SWIR objective lens). We were not only able to observe wave patterns on extraordinary small scales (smallest horizontal wavelength 550 m) but also the formation of a vortex which we interpret as the turbulent breakdown of a wave front (Sedlak et al., 2016).

From October 2017 to June 2019 the instrument observed the area around the Gulf of Trieste from Otlica Observatory, Slovenia (45.93 N, 13.91 °E), which is a partner observatory within the context of the Virtual Alpine Observatory (VAO; <https://www.vao.bayern.de>). This larger data basis includes further observations of small-scale wave features and turbulence which are investigated here.

- 100 The focus of this paper is on analysing small-scale dynamics in the UMLT region in FAIM 3 images with regard to two aspects:
1. A statistical analysis of wave parameters on scales below 4.5 km using a 2-dimensional Fast Fourier Transform (2d-FFT). Using the same measurement technique and analysis we are able to directly connect to the short-scale end of the investigations performed by Hannawald et al. (2019).
 2. The estimation of dissipated energy by analyzing multiple episodes of turbulence (such as the one exemplarily presented in Sedlak et al., 2016).
- 105

2 Instrumentation

FAIM 3 is an OH* airglow imager that has been put into operation in February 2016 at the German Aerospace Center (DLR) in Oberpfaffenhofen, Germany. It consists of the SWIR camera CHEETAH CL manufactured by Xenics nv, which has a thermodynamically cooled 640x512 pixels InGaAs sensor array (pixel size 20 μm x 20 μm, operating temperature 233 K). The camera is sensitive to electro-magnetic radiation in the wavelength range from 0.9 to 1.7 μm (for further technical details see Sedlak et al., 2016).

110

From 26 October 2017 to 6 June 2019 automatic measurements with focus on the OH* airglow emissions have been performed at Otlica Observatory (OTL) (45.93 N, 13.91 °E), Slovenia. FAIM 3 was aligned at a zenith angle of 35° and an azimuthal direction of 240° (facing approximately into WSW direction). Measurements are only possible during night-time because OH* emissions are not detectable in the presence of the much stronger solar radiation. A baffle was attached to prevent the images from being disturbed by reflections from the lab interior, e.g., by moon light. As in Sedlak et al. (2016) the camera was equipped with a 100 mm SWIR lens by Edmund Optics® with aperture angles of 7.3° and 5.9° in horizontal and vertical direction. Neglecting the curvature of the Earth, this configuration leads to a trapezium-shaped field of view (FOV) with a size of ca. 182 km² (13.1–14.1 km x 13.4 km) at the mean peak emission height of the OH* layer at ca. 87 km. The mean spatial resolution is therefore 24 m pixel⁻¹. Due to the abovementioned measurement geometry the FOV is located above the Gulf of Trieste. The integration time of FAIM 3 is 2.8 s, which leads, depending on the season, to the acquisition of ca. 10,000 to 18,000 images per night.

115

120

3 Data Basis

125 All in all, in 477 nights image data were acquired by FAIM 3 at OTL. Since OH* airglow observations are only possible under clear sky conditions, cloudy episodes are sorted out by analyzing keograms. This yields 410 clear sky episodes (durations between 20 min and 13 h) that are distributed over 286 measurement nights. Thus, ca. 60% of the acquired nights at OTL include suitable OH* observations.

Before being analysed, the images undergo the same preprocessing steps as in Hannawald et al. (2016, 2019) and Sedlak et al. (2016): a flat-field correction is performed and the images are transformed to an equidistant grid, which corresponds to a trapezium-shaped FOV due to the inclination from zenith. For each episode the average image is subtracted to ensure that all remnants of fixed patterns are removed (e.g., reflections of the objective lens in the laboratory window during bright nights). Due to the small FOV of FAIM3 we renounce the application of a star removal algorithm to avoid an interpolation of too many pixels. In order to extract periodic signatures a two-dimensional Fast Fourier Transform (2d-FFT) is applied to squared cut-outs of each image, so that neither dimension is favored by the analysis. These cut-outs were chosen to have a side length of 406 pixels (equals ca. 9.7 km) as this is the largest possible square fitting into the transformed images. The 2d-FFT is performed on the squared image cut-out as described by Hannawald et al. (2019). A fitted linear intensity gradient is subtracted from the input images and a Hann window is applied during the 2d-FFT to reduce leakage effects. A local maximum filter is applied to automatically find peaks in the spectra and thus plane wave structures, which allows identifying and analyzing single wave events. Zero-padding on the images is used to improve this identification of peaks in the spectra. Hannawald et al. (2019) present a statistical analysis of gravity waves with horizontal wavelengths between 2 and 62 km (with focus on waves with horizontal wavelengths larger than 15 km). With FAIM 3 having a smaller FOV and a higher spatial resolution than the FAIM instrument used therein, we are now able to present statistics of gravity wave parameters that tie in almost seamlessly with the statistics of longer-scale waves of Hannawald et al. (2019): due to the spatial resolution and the FOV size we cover the horizontal wavelength range from 48 m to 4.5 km. Wave structures with horizontal wavelengths of half the FOV size still showed a strong bias toward phases 0 or π . Extensive testing showed that this effect disappeared when lowering the upper wavelength limit to 4.5 km.

Observed wave structures have to meet several quality criteria in order to be considered a wave event. A wave structure has to be present for at least 20 s and has to be found in at least eight images. This is in contrast to Hannawald et al. (2019) who demand wave signatures to be present for at least 120 s and to appear in at least 100 images within this episode, stating that these restrictions specifically filter out many transient and small-scale wave features as they want to focus on larger persistent waves.

Furthermore, FAIM 3 wave events are considered if they have an amplitude of at least 25% of the maximum observed wave amplitude. Wave structures with this amplitude can just be recognized in the image by the eye. Demanding all the quality criteria mentioned above a total number of 5697 wave events remains. Further restricting these criteria has not significantly

altered the distributions of the wave parameters that are presented in the following. An exemplary event and the respective 2-dimensional spectrum are shown in Figure 1.

We often observe episodes of turbulence in our image series that exhibit the typical dynamics of vortex formation and quasi-chaotic behavior. While the identification of wave structures is done automatically by the 2d-FFT, finding turbulent vortices

160 is done by hand. Turbulent eddy formation can be well recognized by eye when viewing the episodes in the dynamical course of a video sequence. However, the combined effect of these vortices having a certain variety of shapes and sizes, being almost invisible in single images without comparison to preceding or successive images, and causing (compared to other features such as wave fronts) rather small brightness fluctuations in the images hampers strongly the application of image recognition algorithms. For the given data basis 45-25 episodes of turbulence with sufficient quality to derive vortex-turbulence parameters

165 are found. The dates along with the respective turbulence parameters are summarized in Table 1.

~~For both, gravity wave statistics (section 4.1) and the calculation of the energy dissipation rate (section 4.2) the BV frequency is required, which is adapted from the climatology presented by Wüst et al. (2020). It is based on TIMED SABER (Thermosphere Ionosphere Mesosphere Energetics Dynamics, Sounding of the Atmosphere using Broadband Emission Radiometry) temperature data and takes into account the seasonal variability of the angular BV frequency. The climatology of the grid point (45° N, 10° E) is used, which is closest to our FOV. Depending on the day of the year (DoY) the BV frequency is given by~~

170

$$N = 2.20 \cdot 10^{-2} \text{s}^{-2} + 0.19 \cdot 10^{-2} \text{s}^{-2} \sin\left(\frac{2\pi}{324.51 \text{d}} \cdot \text{DoY} - 2.02\right) + 0.05 \cdot 10^{-2} \text{s}^{-2} \sin\left(\frac{2\pi}{180.00 \text{d}} \cdot \text{DoY} + 1.61\right). \quad (3)$$

~~We use an uncertainty of $\pm 5\%$ as according to Wüst et al. (2020) 91% of their data lie within this range around the harmonic approximation. The BV period is then referred to as $\tau_{BV} = \frac{2\pi}{N}$.~~

175 4 Results

4.1 Statistics of Wave Parameters

The wave statistics are presented in Figure 2~~Figure 1~~. Please note that we are using the word ‘wave’ for all wave-like structures we find in the images. The question whether these are actual gravity waves is discussed in section 5. For each wave event the individual BV period is calculated based on Eq. (3) and the DoY. Ca. 63% of the observed wave events have a period longer than the respective BV period and will be referred to as gravity wave events in the following. Their statistical contribution is highlighted in grey in Figure 1.

180

Wave periods range from 21 s to 1498 s (25 min). The median wave period is 359 s (6 min). The median value of gravity wave periods is found at 517 s (8.6 min). The maximum phase speed is 17.6139.8 ms^{-1} with an average value of 7.913.3 ms^{-1} and a standard deviation of 310.3 ms^{-1} . As concerns the zonal distribution, 50.752.7% (49.347.3%) of the gravity-wave events have an eastward (westward) component (consequently no gravity-waves with zonal phase speed zero have been observed) and the mean velocity in eastward (westward) direction is 5.49.4 ms^{-1} (5.38.2 ms^{-1}) with a standard deviation of 3.08.9 ms^{-1} (3.17.4 ms^{-1})

185

1). We find a small seasonal effect in the distribution of zonal phase speeds: ~~53.856.0~~% of the waves have an eastward component and ~~46.244.0~~% a westward component when only considering the winter months December to February while during summer from June to August ~~47.949.5~~% of the waves have an eastward component and ~~52.150.5~~% a westward component. In meridional direction ~~44.442.0~~% (~~53.555.7~~%) of the gravity wave events have a northward (southward) component and the mean meridional phase speed is ~~4.77.5~~ m s^{-1} (~~5.39.4~~ m s^{-1}) in northern (southern) direction with a standard deviation of ~~3.07.1~~ m s^{-1} (~~3.28.7~~ m s^{-1}). Events with meridional phase speed zero have not been considered for the mean values.

4.2 Wave Dissipation

To give an impression of the turbulent dynamics we observe, we present four of our turbulence episodes as video supplement.
195 On 16 November 2017, 02:16 UTC, the turbulent breakdown of parts of an extended wave field can be observed (video 1). On 6 December 2017, 00:26 UTC, several fronts seem to be building up and form rotating vortices (video 2). This can be observed even clearer on 14 October 2018, 17:08 UTC, where the residual movement of turbulent features can be well recognized above the general background movement (video 3). On 4 November 2018, 19:18 UTC, breaking wave fronts seem to form rotating structures of nearly cylindrical shape, while these are accompanied by other turbulently moving eddies (video 4).

200 We estimate the turbulent energy dissipation rate ϵ using equation (1). However, in contrast to Chau et al. (2020) who used radar measurements, we only have horizontal information from our airglow imager. Hecht et al. (2021) demonstrate an approach how to apply equation (1) to purely horizontal airglow imager data, which we adapt to our observations in the following. The characteristic length scale L can be read from the images by measuring the size of the turbulent features. The velocity scale is given by the residual velocity v_{res} of these features. In our observations, they are part of larger instability
205 features, which we assume to be advected by the background wind. We determine v_{res} by reading the actual velocity of the turbulent features and subtracting the background movement v_{bg} in the resulting direction. This is exemplarily shown in Figure 4. The two patches highlighted therein are both moving to the upper right direction but are approaching each other. This helps distinguishing background and residual movement.~~The eddy parameters needed for the calculation of the eddy diffusion coefficient (Eq. 1) are determined manually from the image series of the 45 observations of turbulence. It has to be kept in~~
210 ~~mind that we are deriving properties of a three dimensional movement from two dimensional data.~~

~~We assume the vortices to rotate in a perfect circular shape. The lateral expansion creates the impression of a rotating cylinder. Coherently moving structures give indication of the horizontal velocity vector. Unless the rotational axis is aligned perpendicular to the image plane, the three dimensional vortex rotation manifests as more than one coherent structure that is moving against or overtaking each other (see e.g. Sedlak et al., 2016; Figure 6 therein). During data inspection we noticed that~~
215 ~~the orientation of the rotational axis can be aligned in any direction. It tends to be parallel to the image plane when it evolves directly from the crests of a breaking wave. However, we could also observe eddies rotating around an axis aligned almost perpendicular to the image plane. An example of a rotating vortex within a FAIM 3 snapshot on 4 November 2018 at 19:36:41 UTC is displayed in Figure 3a. The rotational axis and the direction of rotation are marked therein and on an actual cylinder (Figure 3b) for clarification. Since it is very difficult to identify a vortex structure in a single picture we have attached~~

220 a video sequence of this episode (Video 1). The vortex radius and velocity are read from the images. Besides measuring the
vortex rotation, it has also to be taken care of the overall image: if additional to the eddy movement all structures in the FOV
are moving into a common direction, this background motion has to be subtracted. In the example shown above the vortex is
advected toward the left corner. The distance between camera and observed vortex is much larger than the expansion of the
vortex along the rotation axis so that falsifications arising from different perspectives of the vortices can be neglected. This
225 principle is illustrated in Figure 4. As the vortices are three dimensional the alignment of the rotational axis should not affect
the value of the vortex parameters in the images: it does not matter if the axis is aligned perpendicular, parallel or in any other
angle to the image plane, the vortex size will be accessible from the two dimensional projection of the image assuming circular
eddy movement. The same holds for the circumferential velocity since both the radius and the circulation time remain
unchanged. However, perfectly circular eddy rotation does not necessarily occur in nature. Deviations from circularity can
230 lead to both over and underestimation of vortex sizes depending on the vortex orientation. Since isotropy is one of the
characteristic properties of turbulent movements one may presume that from a statistical point of view both cases occur equally
so that no systematic error is made.

As stated in section 3 we found ~~45–25~~ episodes of turbulence that allowed the derivation of ~~the vortex radius~~ L and
~~circumferential velocity~~ v_{res} . Using equation (1), the energy dissipation rate is then calculated by $\epsilon = \frac{v_{res}^3}{L}$. The resulting
235 ~~eddy diffusion coefficients~~ K values are shown in Figure 5. We assume a general read-out error of ± 3 pixels, which
corresponds to a distance of ± 72 m. ~~The circumferential velocity~~ Velocities is-are determined by reading the distance a ~~patch~~
~~on the rotating cylinder surface~~ feature covers within an episode of at least ten images, which corresponds to a time span of
28 s. Thus, ~~the circumferential velocity~~ velocities is-are estimated with an error of $\pm 2.6 \text{ m s}^{-1}$. The arising uncertainties of ~~$K\epsilon$~~
are calculated following the rules of error propagation.

240 The values of ~~$K\epsilon$~~ range from ~~0.08 to 1.949.03~~ $\cdot 10^4 \text{ m}^{2\text{s}^{-1}} \text{ W kg}^{-1}$. The ~~mean median~~ value is ~~0.761.45~~ $\cdot 10^4 \text{ m}^2\text{s}^{-1} \text{ W kg}^{-1}$
(standard deviation of ~~0.53~~ $\cdot 10^4 \text{ m}^2\text{s}^{-1}$) and we retrieve a median of ~~0.59~~ $\cdot 10^4 \text{ m}^2\text{s}^{-1}$. It is difficult to exactly quantify the
error of manual parameter determination from the images. However, in this work we rather focus on the order of magnitude
of K . When calculating K two distance values are read from the images (one for the vortex size and one for the determination
of the circumferential speed). Considering Eq. (1), a mistake of factor 10 is made for K if these distances are misread by a
245 factor of at least $\sqrt{10}$. The shortest (and therefore most difficult to determine) diameter in our analysed examples was 768 m.
For an error of one order of magnitude of K this distance must be misread as either shorter than 243 m or longer than 2428 m,
i.e. a distance of 32 pixels must be wrongly interpreted as shorter than 9 pixels or longer than 101 pixels. This lies far beyond
the read-out uncertainty of ± 3 pixels we introduced above and can be assumed to be much worse than any read-out error one
would normally make.

250 The energy dissipation rate ϵ can be estimated from the eddy diffusion coefficient K according to Eq. (2) using the BV
frequency as described by Eq. (3).

As can be seen in Figure 5 the energy dissipation rate of the observed turbulence events is in the range ~~0.63~~ $\text{—} 14.21 \text{ W kg}^{-1}$.

Assuming the duration of dissipation being equal to the lifetime of the vortex the energy dissipation rate can be converted into the amount of dissipated energy per mass. This is only done for those vortices that both form and decay within the FOV. The time intervals of dissipation are between ~~146-241~~s and 922 s (2-4.0–15.4 min) and can also be found in Table 1. Events are labelled as ‘out of FOV’ or as ‘clouds’ if either the formation or the decay of the vortex cannot be observed. No further analysis is performed for these events.

Multiplying energy dissipation rate and duration of dissipation equals the energy per mass that is released in the turbulent process. We retrieve values between ~~220-30~~ and ~~6346-3015~~ J kg⁻¹. Given that the released energy is entirely converted into heat we can make a rough estimate of the resulting temperature change by assuming isobaric conditions (may be approximately fulfilled due to the stable stratification of the atmosphere and small vertical dimension of eddies) and dividing energy per mass by the specific heat capacity of dry air (10³ JK⁻¹ kg⁻¹). The resulting temperature changes in this work are in the range ~~0.032-6.33.02~~ K. ~~64% (21 out of 33) of these values are larger than one Kelvin.~~ All values of dissipated energy per mass and maximum temperature change can be found in Table 1.

Since we now have a time series of eddy diffusion coefficients we can compare them to gravity wave activity in the UMLT above OTL. Parallel to FAIM 3, SWIR spectrometers called GRIPS (GROund-based Infrared P-branch Spectrometer) instruments deliver time series of OH* rotational temperatures derived from the OH(3-1) P-branch (1.5 μm-1.6 μm) at an initial temporal resolution of 15 s. Unlike the general instrument details discussed by Schmidt et al. (2013), the GRIPS9 at OTL has a reduced aperture angle of 6.2°-FWHM increasing its responsivity to smaller structures. As described in Sedlak et al. (2020), gravity wave activity – the so-called significant wavelet intensity (SWI) – for the periods 6-480 min (period resolution 1 min) can be calculated by applying a wavelet analysis to these temperature time series. The FOV of GRIPS9 is also located above the Gulf of Trieste and in ca. 30 km distance to the FAIM 3 FOV and has a size of approximately 13 km x 19 km. Since the spectroscopic observations are averaged over the entire FOV, GRIPS is most sensitive for gravity waves with horizontal wavelengths of several hundreds of kilometres (Wüst et al., 2016). The time series of nocturnal SWI is restricted to those nights that exhibited at least one of the turbulence episodes presented above and the correlation between the SWI and the eddy diffusion coefficient has been calculated. If there are observations of more than one vortex during one night, the respective eddy diffusion coefficients are averaged to their mean value. The Pearson correlation coefficient and the P value (significance test) are presented in Figure 7. We find ~~a slight but almost no~~ significant ~~anti~~correlation for ~~any~~ gravity wave periods ~~in the range 122-207 min. For these periods the mean value of the correlation coefficient is -0.46. The highest coefficient of anticorrelation is -0.52 at a period of 178 min.~~

5 Discussion

~~As can be seen in Figure 3, the wave structures we observed exhibit multiple directions. The strong tendency to north-eastern direction in summer and to the (south-)west in winter as observed by Hannawald et al. (2019) for medium-scale gravity waves cannot be confirmed for the waves observed here. However, slight tendencies are apparent in Figure 3. The north-western~~

285 component these authors observed during winter at Mt. Sonnblick in Austria with the FOV being positioned north of the Alps
also appears in our data during autumn, winter and spring. During summer we find a conspicuous majority of waves
propagating into southern direction.

The number of waves propagating eastward and westward is almost equal for the entire data set. However, as stated in section
4.1, more waves are oriented in eastward direction during winter whereas zonal directions are quite balanced during summer.
290 Although the eastward tendency during winter is quite weak, it contradicts the distribution that is expected for gravity waves
being created in the lower atmosphere and propagating upward, being subdued to tropospheric and stratospheric wind filtering.
The eastward oriented mean wind profile during winter would lead to mainly westward propagating gravity waves reaching
the UMLT without encountering critical levels. During summer the stratospheric winds reverse to westward direction, so that
eastward oriented gravity waves are filtered in the tropopause and westward oriented gravity waves are filtered in the
295 stratosphere (see, e.g., Hoffmann et al., 2010; Hannawald et al., 2019).

As we have no accompanying wind measurements in the height of our observations it is difficult to decide by means of the
period whether the wave structures presented in section 4.1 are small-scale gravity waves or instability features. Ca. 63 % of
the wave events have an observed period above the BV period (here we used the climatology presented by Wüst et al., 2020),
however these could at least in parts also be Doppler-shifted instability features instead of gravity waves. While the distinction
300 between largely extended wave-fields (bands) and small localized wave structures that are related to instability (ripples) is
often made at a horizontal wavelength of 10-20 km (Taylor et al., 1997; Nakamura et al., 1999), Li et al. (2017) remark that
even structures with horizontal wavelengths of 5-10 km may sometimes be gravity waves rather than instability features.

If this would be true for our small-scale wave structures, they might rather be secondary gravity waves (see, e.g., Becker &
Vadas, 2018), being generated at greater heights by breaking gravity waves. Secondary gravity waves can either have larger
305 wavelengths and phase speeds than the primary wave if they are created by localized momentum deposition (Vadas & Becker,
2018) or smaller wavelengths and phase speeds if they are induced by the nonlinear flow (wave-mean flow and wave-wave
interactions; see, e.g., Bacmeister & Schoeberl, 1989; Franke & Robinson, 1999; Bossert et al., 2017). The former type of
secondary gravity waves exhibits a rather broad spectrum of wave parameters with horizontal wavelengths longer than 500 km
and horizontal phase speeds between 50 and 250 ms⁻¹ (Vadas et al., 2018), resulting in periods longer than ca. 30 min. The

310 wave structures found in this work have smaller horizontal wavelengths, phase speeds and periods and could therefore be more
likely related to the latter type of secondary waves created by nonlinearities. However, these small-scale secondary waves are
unlikely to propagate large vertical distances due to their small horizontal phase speeds (Becker & Vadas, 2018). They have
to be generated at even higher altitudes, i.e. close to the mesopause, to be observable with OH* airglow imagers. Hannawald
et al. (2019), e.g., deduce from their observations that not only the zonal stratospheric winds but also the meridional circulation
315 in the mesosphere might play a vital role in filtering gravity waves. The meridional mesospheric circulation is oriented
southward during summer and northward during winter, being much stronger during summer with ca. 10-14 m/s (Yuan et al.,
2008). Simulations by Becker & Vadas (2018) show that advection by the background wind determines the direction of a
newly created secondary wave. Based on these aspects, the accumulation of southward oriented waves we observe during

summer could be a hint for gravity waves being filtered by the mesospheric circulation and generating subsequent secondary waves with shorter wavelengths and periods, that are provided with a southward phase speed due to advection. This theory is also in good agreement with our observed meridional phase speeds: in the abovementioned velocity range of the summerly meridional mesospheric circulation (10-14 m/s) meridional phase speeds are southward in 71 % of cases.

The directions of propagation are quite uniformly distributed over all quadrants as can be seen in Figure 2. The strong tendency to north-eastern direction in summer and to the (south-)west in winter as observed by Hannawald et al. (2019) for medium-scale gravity waves cannot be confirmed for the waves observed here. Only the north-western component these authors observed during winter at Mt. Sonnblick in Austria with the FOV being positioned north of the Alps also appears in our data during autumn, winter and spring. During summer we find a conspicuous majority of waves propagating into southern direction.

The number of waves propagating eastward and westward is almost equal for the entire data set. However, as stated in section 4.1, more waves are oriented in eastward direction during winter (positive zonal phase speed) and in westward direction during summer. Although this tendency is quite weak, it contradicts the distribution that is expected for gravity waves being created in the lower atmosphere and propagating upward, being subdued to stratospheric wind filtering. The eastward-oriented mean wind profile during winter would lead to mainly westward propagating gravity waves reaching the UMLT without encountering critical levels. The reversed stratospheric winds during summer would consequently allow some more eastward travelling gravity waves to propagate upward (see e.g. Hoffmann et al., 2010; Hannawald et al., 2019). Since the highest observed phase speed of waves with periods longer than the BV period is only 17.6 m s^{-1} , it can be assumed that in the majority we do not observe gravity waves that are originating from low altitudes and are fast enough not to be blocked by the stratospheric wind fields.

Considering the directional distribution, it is possible that the major part of our waves may be secondary gravity waves (see e.g. Becker & Vadas, 2018), being generated at greater heights by breaking gravity waves. Secondary gravity waves can either have larger wavelengths and phase speeds than the primary wave if they are created by localized momentum deposition (Vadas & Becker, 2018) or smaller wavelengths and phase speeds if they are induced by the nonlinear flow (wave mean flow and wave-wave interactions; see e.g. Baumeister & Schoeberl, 1989; Franke & Robinson, 1999; Bossert et al., 2017). The former type of secondary gravity waves exhibits a rather broad spectrum of wave parameters with horizontal wavelengths longer than 500 km and horizontal phase speeds between 50 and 250 m s^{-1} (Vadas et al., 2018), resulting in periods longer than ca. 30 min. The wave structures found in this work have smaller horizontal wavelengths, phase speeds and periods and could therefore be more likely related to the latter type of secondary waves created by nonlinearities. However, these small scale secondary waves are unlikely to propagate large vertical distances due to their small horizontal phase speeds (Becker & Vadas, 2018). They have to be generated at even higher altitudes, i.e. close to the mesopause, to be observable with OH* airglow imagers. Hannawald et al. (2019) e.g. deduce from their observations that not only the zonal stratospheric winds but also the meridional circulation in the mesosphere might play a vital role in filtering gravity waves. The meridional mesospheric circulation is oriented southward during summer and northward during winter, being much stronger during summer with ca. 10-14 m/s

(Yuan et al., 2008). Simulations by Becker & Vadas (2018) show that advection by the background wind determines the direction of a newly created secondary wave. Based on these aspects, the accumulation of southward-oriented waves we observe during summer could be a hint for gravity waves being filtered by the mesospheric circulation and generating subsequent secondary waves with shorter wavelengths and periods, that are provided with a southward phase speed due to advection. This theory is also in good agreement with our observed meridional phase speeds: in the abovementioned velocity range of the summery meridional mesospheric circulation (10–14 m/s) meridional phase speeds are southward in 62% of cases.

However, regarding the small horizontal wavelengths below 4.5 km, it is more likely that the major part of the observations presented in section 4.1 are related to instability features. The quite slow phase speeds (mean value 13.3 m/s) are one hint for this as typical gravity wave phase speeds accumulate around 40 m/s (see, e.g., Wachter et al., 2015 and Wüst et al., 2018). If Figure 3b was the phase speed distribution of gravity waves, it is likely that a majority of them would encounter critical levels somewhere and would not be observable in the OH* layer. The small spatial scales of the wave structures we observe are also typical for ripple structures as they were already observed with FAIM 3 (Sedlak et al., 2016). Their short life spans are not excluded by our quality criteria. Tuan et al. (1979) state that oscillations of this type are usually excited at periods of 4–10 min, which would explain the large number of wave events we observe in this period range. Observing ripple structures, it would not be surprising to obtain a certain diversity of directions of propagation. In principle, ripples originating from convective instabilities tend to be aligned perpendicular to the wave fronts of the initial wave, whereas ripples arising from dynamic instabilities form parallel to the initial wave fronts (Andreassen et al., 1994; Fritts et al., 1997; Hecht et al., 2000). However, it has been reported that ripples can be rotated by the background wind and that ripples may even be created by a combination of both dynamical and convective instability (Fritts et al., 1996; Hecht, 2004). Considering the fact that the directional peculiarities of our observed wave events fit well with the expected behavior of secondary gravity waves, as discussed above, support the scenario of the wave structures being ripples from dynamic instabilities of secondary gravity waves, that originate from the stratospheric and mesospheric jet. Capturing structures related to instability is not unlikely, considering the numerous observations of turbulent vortices with the FAIM 3 setup.

Li et al. (2017) report that ripples are hard to distinguish from small scale gravity waves. Height-resolved measurements of the horizontal wind would be needed to determine the local wind shear and make a profound statement about atmospheric instability. Nevertheless, height-resolved measurements of the horizontal wind would be needed to determine the local wind shear and make a profound statement about atmospheric instability. capturing structures related to instability is not unlikely, considering the numerous observations of turbulent vortices with the FAIM 3 setup.

It has to be kept in mind that a 2d-FFT was used. Thus, periodic structured are assumed to be stationary, i.e., they extend over the entire image. Faint structures that appear only in small parts of the image (as does for example the 550m wave packet in Sedlak et al., 2016; Fig. 2) would be underrepresented by this analysis.

There are still very few measurements of turbulent eddy diffusion coefficients in the Measuring the eddy diffusion coefficient in the UMLT is still challenging and there are only few studies yet. Rocket measurements -of Lübken (1997) reports K to be

around deliver energy dissipation rates between ca. 0.01 and 0.1 W kg^{-1} at a height of 87 km at between 85 and 90 km height at high latitudes. Chau et al. (2020) find an energy dissipation rate of 1.125 W kg^{-1} for their KHI event observed in the summer mesopause and state that this is a rather high value compared to the findings of Lübken et al. (2002). Hocking (1999) provides a rescaled overview of earlier values of the energy dissipation rate and these have a maximum magnitude of 0.1 W kg^{-1} . Hecht et al. (2021) derive a value of 0.97 W kg^{-1} from airglow images of a KHI event. Hodges (1969) states that the eddy diffusion coefficient caused by gravity waves is typically around $10^2 \text{ m}^2 \text{ s}^{-1}$. According to the CIRA (Committee on Space Research (COSPAR) International Reference Atmosphere) climatology of 1986 (NASA National Space Science Data Center, 2007) global values range between magnitudes of 10^2 and $10^3 \text{ m}^2 \text{ s}^{-1}$. LIDAR measurements above New Mexico, USA deliver values that vary strongly around a magnitude of $10^2 \text{ m}^2 \text{ s}^{-1}$ (Liu, 2009). Smith (2012) notes that the WACCM (Whole Atmosphere Community Climate Model) climatology exhibits rather small values with magnitude $10^1 \text{ m}^2 \text{ s}^{-1}$ and that the huge discrepancies of K estimates cannot be fully explained yet. Ranging from 0.08 up to 9.03 W kg^{-1} the values of energy dissipation rate derived here are higher than reported by other studies. However, the median value of 1.45 W kg^{-1} is not too far away from the values of Chau et al. (2020) and Hecht et al. (2021). The here-presented values of K exhibit a magnitude of $10^3 - 10^4 \text{ m}^2 \text{ s}^{-1}$, which partly agrees with recent results, although some of our values are higher. The vortices we observe do not necessarily mark the small-scale end of the energy cascade. It could be possible that the energy is cascaded further to a larger number of smaller eddies that are no longer visible to our instrument. Parallel in-situ measurements (e.g., lidar, rockets) could be used to estimate the significance of this effect. Additionally, it has to be kept in mind that – except for the studies of Hecht et al. (2021), whose value is quite similar to the median value of our data – the values compared here arise from different measurement techniques with different horizontal, vertical and temporal resolutions, so that the accessible scales are not necessarily identical due to the observational filter effect. Nevertheless, the agreement of the above mentioned authors on eddy parameters in the UMLT is quite good, considering the fact that energy dissipation rate in the upper troposphere and lower stratosphere varies by a factor of more than five orders of magnitude (Li et al., 2016). The derivation of the vortex turbulence parameters performed here is challenging due to the blurred shape of dynamic signatures in the OH* layer. Circumferential speed and vortex radius The length scale and velocity scale of turbulent features have been extracted manually by measuring distances in the images and calculating distances from pixel values, and we We tried to quantify the read-out error by providing a measurement uncertainty and minimize it by repeating the analysis workflow on the same data multiple times. However, using equation (1) velocity dominates the length scale due to its power of 3, so that ϵ strongly depends on a parameter, which is quite difficult to extract from the images. All in all, it seems possible to derive turbulence parameters like the eddy diffusion coefficient and energy dissipation rate from high resolution imager data. The values of eddy diffusion coefficients energy dissipation rate derived here show no significant anticorrelation with gravity wave activity in the period range $122.6 - 207.480 \text{ min}$. Turbulence thus cannot be related to distinct periods of the gravity wave spectrum with the here-presented data. One may assume that turbulent vortices we observe could be predominantly attributed to breaking gravity waves in this period range. If this was the case, stronger wave breaking would manifest as higher eddy diffusion coefficients and result in a lower activity of gravity waves with periods $122 - 207 \text{ min}$ in the UMLT. However, A

larger data basis of turbulence parameters and especially observations of period-resolved gravity wave activity at altitudes below ~~would~~ will be needed to ~~confirm this assumption~~ answer the question if all parts of the gravity wave spectrum drive turbulence generation in the UMLT equally.

425 Assuming that the turbulently dissipated energy is entirely converted into heat we find temperature changes of 0.03-3.02 K~~0.2-6.3 K~~ that occur within time spans of 2.4~~0~~-15.4 min. Marsh (2011) report chemical heating rates in the atmosphere to be around 3-4K per day. Given that our analysed episodes are typical representatives of turbulent wave breaking, dynamical heating by gravity wave dissipation would deliver the same effect within few minutes at very localized areas in the UMLT as does chemical heating during an entire day for the whole atmosphere.

6 Summary

430 We present an analysis of small-scale ~~wave~~ dynamics of instability features and turbulence from OH* imager data acquired between 26 October 2017 and 6 June 2019 at Otlica Observatory, Slovenia. Measurements have been performed with the imager FAIM 3, which has a spatial resolution of ca. 24 m pixel⁻¹ and a temporal resolution of 2.8 s.

Wave-like structures in the images are systematically identified by applying a 2d-FFT to nocturnal image sequences during clear sky episodes. All ~~wave~~ events meeting our persistency criteria were used to derive a statistical analysis of wave-like 435 structures with horizontal wavelengths between 48 m and 4.5 km. The small horizontal scales are a strong hint that these are likely instability features of breaking gravity waves like ripples. ~~63% of the wave events have a period longer than the BV period and may be tentatively considered as gravity waves.~~ We ~~find an isotropic distribution of~~ generally find variable directions of propagation, which indicates that these wave-like structures may be mostly created above the stratospheric wind fields. However, a weak seasonal dependency is found: zonal directions of ~~wave~~ propagation are slightly more eastward during 440 winter and westward during summer. We speculate these to be instability features generated by breaking secondary gravity waves ~~in the course of wind filtering~~, receiving their zonal direction through advection by the background wind. We find a stronger tendency of southward propagation during summer, which may point to a vital role of gravity wave filtering and excitation of secondary waves and their subsequent instability features by the meridional mesospheric circulation. ~~It is possible that secondary waves and instability features represent the majority of our observed waves.~~

445 Furthermore, we observed and presented OH* imager observations of turbulence with high spatio-temporal resolution. We estimated turbulence parameters from 245 episodes of ~~vortex eddy~~ observations. ~~The derived values of eddy diffusion coefficients are in the range around 10³-10⁴ m²s⁻¹ and agree mostly with earlier results from rocket and lidar measurements and simulations. Considering the respective values of the BV frequency as calculated by Wüst et al. (2020) Following the approach of Hecht et al. (2021) we retrieve~~ derived the energy dissipation rates for our observed events by reading the turbulent 450 length and velocity scale from the image series. Our values range between 0.08 and 9.03 W kg⁻¹; and are higher than earlier rocket measurements. The values presented here would ~~that~~ cause ~~estimated-localized~~ heatings ~~by of 0.03-3.02 K~~ 0.2-6.3 K per turbulence event. ~~These have the~~ The largest of these reach the same order of magnitude as the daily chemical heating rates

as reported by Marsh (2011). Given that the observed events are representative of typical processes of gravity wave dissipation, this emphasizes the importance of carefully integrating gravity wave turbulence into climate simulations.

455 Being able to derive reasonable values of UMLT turbulence parameters from imager data represents an important progress for measurement techniques of atmospheric dynamics. Airglow imagers are much cheaper and more flexible than rockets or lidars. Considering the huge amount of data, artificial intelligence could be used in the future to identify and analyse turbulent episodes.

Appendix A

460 Derivation of the eddy diffusion coefficient K (Eq. (1))

The derivation of the eddy diffusion coefficient shown here is based on Prölss (2001). It is assumed that a cylindrical vortex with radius r_e and cylinder height d is excited in the course of turbulence, which rotates around an axis perpendicular to the circular cylinder bases (Figure 8). We consider an atmosphere of particle number density n (varying with height z) in which a

465 side gas i with particle number density n_i exhibits a concentration gradient $\frac{d(\frac{n_i}{n})}{dz}$ (concentration as ratio of particle numbers of side gas and total atmosphere) perpendicular to the rotational axis. Maximum mixing results when the cylinder rotates half a turn, i.e. when the cylinder segment of high concentration and the cylinder segment of low concentration switch places. This induces a net particle flux through the center plane A of the cylinder.

Let us consider two cylinder segments 1 and 2 of thickness ds , width $2b$ and depth d at distance $\pm s$ from the center plane, thus having the volume $dV = d 2b ds$. The number of side gas particles they contain is

$$(dN_i)_\pm = dV n_\pm \left(\frac{n_i}{n}\right)_\pm \quad (4)$$

and

$$(dN_i)_z = dV n_z \left(\frac{n_i}{n}\right)_z = dV n_z \left[\left(\frac{n_i}{n}\right)_\pm + \frac{d(\frac{n_i}{n})}{dz} 2s + \dots \right]. \quad (5)$$

475 During half a vortex rotation the segments 1 and 2 move towards the center plane. n and n_i change with height while $\frac{n_i}{n}$ remains constant ($n(z) = n$ at the center plane). This results in a net exchange of

$$(dN_i)_A = [(dN_i)_\pm - (dN_i)_z]_A \approx -dV n \frac{d(\frac{n_i}{n})}{dz} 2s \quad (6)$$

side gas particles through the center plane $A = 2r_e d$ (i.e. we subtracted Eq. (5) from Eq. (4)). With a circumferential velocity v_e and an exchange time of $\Delta t = \frac{\pi r_e}{v_e}$ for half a rotation this leads to a differential particle flux density of

$$d\Phi_e = \frac{(dN_i)_A}{A \Delta t} = -dV n \frac{d(\frac{n_i}{n})}{dz} 2s \frac{1}{A \Delta t} = -d 2b ds n \frac{d(\frac{n_i}{n})}{dz} 2s \frac{1}{2r_e d \frac{\pi r_e}{v_e}} = -2\sqrt{r_e^2 - s^2} ds n \frac{d(\frac{n_i}{n})}{dz} s \frac{1}{r_e \pi r_e}. \quad (7)$$

480 Please note that b has been replaced by $\sqrt{r_e^2 - s^2}$ according to the Pythagoras Theorem.

Integration over all cylinder segments yields the total flux density

$$\Phi_e = \int_{s=0}^{r_e} d\Phi_e = -\frac{2}{\pi} \frac{v_e}{r_e^2} n \frac{d\left(\frac{n_e}{n}\right)}{dz} \int_{s=0}^{r_e} \sqrt{r_e^2 - s^2} s ds. \quad (8)$$

The integral can be solved by substituting $x := r_e^2 - s^2$ and therefore $\frac{dx}{ds} = -2s$.

Then

$$485 \int_{s=0}^{r_e} \sqrt{r_e^2 - s^2} s ds = -\frac{1}{2} \int_{r_e^2}^0 \sqrt{x} dx = -\frac{1}{3} \left[x^{\frac{3}{2}} \right]_{r_e^2}^0 = \frac{1}{3} r_e^3 \quad (9)$$

so that

$$\Phi_e = -\frac{2}{3\pi} r_e v_e n \frac{d\left(\frac{n_e}{n}\right)}{dz}. \quad (10)$$

Analogously to Fick's law of molecular diffusion we can write the flux density of eddy diffusion as

$$\Phi_e = -K n \frac{d\left(\frac{n_e}{n}\right)}{dz} \quad (11)$$

490 where

$$K = \frac{2}{3\pi} r_e v_e$$

is the eddy diffusion coefficient.

Data availability

495 The data are archived at the WDC-RSAT (World Data Center for Remote Sensing of the Atmosphere). The FAIM and GRIPS instruments are part of the Network for the Detection of Mesospheric Change, NDMC (<https://ndmc.dlr.de>).

Author contribution

The conceptualisation of the project, the funding acquisition as well as the administration and supervision were done by MB and SW. The operability of the instrument was assured by RS. SS provided us the opportunity to set up our instrument at Otlica
500 Observatory and took care of the maintenance. The algorithm for retrieving wave statistics was written by PH. The analyses of wave statistics and turbulence from FAIM 3 images as well as the visualization of the results were performed by RS. Setup, operation and data reduction for GRIPS9 was done by CS. The interpretation of the results benefited from fruitful discussions between PH, CS, SW, MB, and RS. The original draft of the manuscript was written by RS. Careful review of the draft was performed by all co-authors.

505 **Competing interests**

The authors declare that they have no conflict of interest.

Acknowledgement

This research received funding from the Bavarian State Ministry of the Environment and Consumer Protection by grant number TKP01KPB-70581 (Project VoCaS-ALP).

510 **References**

- Adams, G. W., Peterson, A. W., Brosnahan, J. W., and Neuschaefer, J. W.: Radar and optical observations of mesospheric wave activity during the lunar eclipse of 6 July 1982, *J. Atmos. Terr. Phys.*, 50, 11–20, 1988.
- Andreassen, Ø., Wasberg, C. E., Fritts, D. C., and Isler, J. R.: Gravity wave breaking in two and three dimensions 1. Model description and comparison of two-dimensional evolutions, *J. Geophys. Res.*, 99, 8095–8108, 1994.
- 515 Bacmeister, J. T., & Schoeberl, M. R.: Breakdown of vertically propagating two-dimensional gravity waves forced by orography, *J. Atmos. Sci.*, 46, pp. 2109–2134., 1989.
- Baker, D. J. and Stair, A. T.: Rocket Measurements of the Altitude Distributions of the Hydroxyl Airglow, *Phys. Scripta*, 37, 611–622, <https://doi.org/10.1088/0031-8949/37/4/021>, 1988.
- Baumgarten, G. and Fritts, D. C.: Quantifying Kelvin-Helmholtz instability dynamics observed in noctilucent clouds: 1. 520 Methods and observations, *J. Geophys. Res. Atmos.*, 119, pp. 9324–9337, doi:10.1002/2014JD021832, 2014.
- Becker, E. and Vadas, S. L.: Secondary Gravity Waves in the Winter Mesosphere: Results From a High-Resolution Global Circulation Model, *J. Geophys. Res.: Atmospheres*, 123, pp. 2605–2627, <https://doi.org/10.1002/2017JD027460>, 2018.
- Beldon, C. L., and Mitchell, N. J.: Gravity waves in the mesopause region observed by meteor radar, 2: Climatologies of 525 gravity waves in the Antarctic and Arctic, *J. Atmos. Sol.-Terr. Phy.*, 71, pp. 875–884, <https://doi.org/10.1016/j.jastp.2009.03.009>, 2009.
- Bittner, M., Offermann, D., and Graef, H. H.: Mesopause temperature variability above a midlatitude station in Europe, *J. Geophys. Res.*, Vol. 105, pp. 2045–2058, 2000.
- Bossert, K., Kruse, C. G., Heale, C. J., Fritts, D. C., Williams, B. P., Snively, J. B., Pautet, P.-D., and Taylor, M. J.: . Secondary 530 gravity wave generation over New Zealand during the DEEPWAVE campaign. *Journal of Geophysical Research: Atmospheres*, 122, pp. 7834–7850, <https://doi.org/10.1002/2016JD026079>, 2017.
- Browning, K. A.: Structure of the atmosphere in the vicinity of large-amplitude Kelvin–Helmholtz billows, *Q. J. Roy. Meteor. Soc.*, 97, 283–299, 1971.

- 535 [Chau, J. L., Urco, J. M., Avsarkisov, V., Vierinen, J. P., Latteck, R., Hall, C. M., and Tsutsumi, M.: Four-Dimensional Quantification of Kelvin-Helmholtz Instabilities in the Polar Summer Mesosphere Using Volumetric Radar Imaging, *Geophys. Res. Lett.*, 47, e2019GL086081, <https://doi.org/10.1029/2019GL086081>, 2020.](#)
- de la Cámara, A., Lott, F., and Abalos, M.: Climatology of the middle atmosphere in LMDz: Impact of source-related parameterizations of gravity wave drag, *J. Adv. Model. Earth Syst.*, 8, 1507-1525, doi:10.1002/2016MS000753, 2016.
- 540 Espy, P. J., and Stegman, J.: Trends and variability of mesospheric temperature at high-latitudes, *Phys. Chem. Earth*, 27, pp. 543-553, 2002.
- Espy, P. J., Hibbins, R. E., Jones, G. O. L., Riggan, D. M., and Fritts, D. C.: Rapid, large-scale temperature changes in the polar mesosphere and their relationship to meridional flows, *Geophys. Res. Letters*, Vol. 30, No. 5, 1240, doi:10.1029/2002GL016452, 2003.
- 545 Franke, P. M. and Robinson, W. A.: Nonlinear behaviour in the propagation of atmospheric gravity waves, *J. Atmos. Sci.*, 56, pp. 3010-3027, 1999.
- French, W. J. R., and Burns, G. B.: The influence of large-scale oscillations on long-term trend assessment in hydroxyl temperatures over Davis, Antarctica, *J. Atmos. Sol.-Terr. Phys.*, 66, pp. 493-506, doi:10.1016/j.jastp.2004.01.027, 2004.
- Fritts, D. C. and Alexander, M. J.: Gravity wave dynamics and effects in the middle atmosphere, *Review of Geophysics*, 41, 550 1, doi:10.1029/2001RG000106, 2003.
- Fritts, D. C., Garten, J. F., and Andreassen, Ø.: Wave breaking and transition to turbulence in stratified shear flows, *J. Atmos. Sci.*, 53, 1057–1085, 1996.
- Fritts, D. C., J. R. Isler, J. H. Hecht, R. L. Walterscheid, and O. Andreassen: Wave breaking signatures in sodium densities and OH nightglow. 2. Simulation of wave and instability structures, *J. Geophys. Res.*, 102, 6669–6684, 555 doi:10.1029/96JD01902, 1997.
- Gardner, C. S., Zhao, Y., and Liu, A. Z.: Atmospheric stability and gravity wave dissipation in the mesopause region, *J. Atmos. Sol.-Terr. Phys.*, 64, 923–929, 2002.
- [Gargett, A. E.: Velcro Measurement of Turbulence Kinetic Energy Dissipation Rate \$\epsilon\$, *Journal of Atmospheric and Oceanic Technology*, 16, pp. 1973-1993, 1999.](#)
- 560 Hannawald P., Schmidt, C., Wüst, S., and Bittner, M.: A fast SWIR imager for observations of transient features in OH airglow, *Atmos. Meas. Tech.*, 9 1461-1472, doi:10.5194/amt-9-1461-2016, 2016.
- Hannawald, P., Schmidt, C., Sedlak, R., Wüst, S., and Bittner, M.: Seasonal and intra-diurnal variability of small-scale gravity waves in OH airglow at two Alpine stations, *Atmos. Meas. Tech.*, 12,457–469, DOI: 10.5194/amt-12-457-2019, 2019.
- 565 Hecht, J. H., Walterscheid, R. L., Fritts, D. C., Isler, J. R., Senft, D. C., Gardner, C. S., and Franke, S. J.: Wave breaking signatures in OH airglow and sodium densities and temperatures 1. Airglow imaging, Na lidar, and MF radar observations, *J. Geophys. Res.*, Vol. 102, No. D6, pp. 6655-6668, 1997.

- Hecht, J. H., C. Fricke-Begemann, R. L. Walterscheid, and J. Höffner: Observations of the breakdown of an atmospheric gravity wave near the cold summer mesopause at 54N, *Geophys. Res. Lett.*, 27, 879–882, doi:10.1029/1999GL010792, 2000.
- 570 Hecht, J. H.: Instability layers and airglow imaging, *Review of Geophysics*, Vol. 42, 2004.
- Hecht, J. H., Wan, K., Gelinas, L. J., Fritts, D. C., Walterscheid, R. L., Rudy, R. J., Liu, A. Z., Franke, S. J., Vargas, F. A., Pautet, P. D., Taylor, M. J., and Swenson, G. R.: The life cycle of instability features measured from the Andes Lidar Observatory over Cerro Pachon on 24 March 2012, *J. Geophys. Res. Atmos.*, 119, 8872–8898, 2014.
- 575 [Hecht, J. H., Fritts, D. C., Gelinas, L. J., Rudy, R. J., Walterscheid, R. L., and Liu, A. Z.: Kelvin-Helmholtz Billow Interactions and Instabilities in the Mesosphere Over the Andes Lidar Observatory: 1. Observations, *JGR Atmospheres*, 126, e2020JD033414. <https://doi.org/10.1029/2020JD033414>, 2021.](https://doi.org/10.1029/2020JD033414)
- Hines, C.O. and Tarasick, D.W.: On the detection and utilization of gravity waves in airglow studies, *Planet. Space Sci.*, 35, 851–866, [https://doi.org/10.1016/0032-0633\(87\)90063-8](https://doi.org/10.1016/0032-0633(87)90063-8), 1987.
- Hocking, W. K.: Measurement of turbulent energy dissipation rates in the middle atmosphere by radar techniques: A review, *Radio Sci.*, 20, 6, pp. 1403-1422, 1985.
- 580 [Hocking, W. K.: The dynamical parameters of turbulence theory as they apply to middle atmosphere studies, *Earth Planets Space*, 51, pp. 525-541, 1999.](#)
- ~~[Hodges, R. R.: Eddy diffusion coefficients due to instabilities in internal gravity waves, *J. Geophys. Res.*, 74, Issue 16, pp. 4087-4090, 1969.](#)~~
- 585 Hoffmann P., Becker, E., Singer, W., and Placke, M.: Seasonal variation of mesospheric waves at northern middle and high latitudes, *J. Atmos. Sol.-Terr. Phy.*, 72, pp. 1068-1079, 2010.
- Holton, J. R.: The influence of gravity wave breaking on the general circulation of the middle atmosphere, *J. Atmos. Sci.*, 40, pp. 2497-2507, 1983.
- Holton, J. R. and Alexander, M. J.: Gravity waves in the mesosphere generated by tropospheric convection, *Tellus*, 51A-B, 590 pp. 45-58, 1999.
- Li, Z., Liu, A. Z., Lu, X., Swenson, G. R., and Franke, S. J.: Gravity wave characteristics from OH airglow imager over Maui, *J. Geophys. Res.*, Vol. 116, Issue D22, 2011.
- 595 ~~[Li, Q., Rapp, M., Schrön, A., Schneider, A., and Stober, G.: Derivation of turbulent energy dissipation rate with the Middle Atmosphere Alomar Radar System \(MAARSY\) and radiosondes at Andøya, Norway, *Ann. Geophys.*, 34, pp. 1209-1229, doi:10.5194/angeo-34-1209-2016, 2016.](#)~~
- Li, J., Li, T., Dou, X., Fang, X., Cao, B., She, C.-Y., Nakamura, T., Manson, A., Meek, C., and Thorsen, D.: Characteristics of ripple structures revealed in OH airglow images, *J. Geophys. Res. Space Physics*, 122, pp. 3748-3759, doi:10.1002/2016JA023538, 2017.
- Lindzen, R. S.: Turbulence and stress owing to gravity wave and tidal breakdown, *J. Geophys. Res.: Oceans banner*, 86, C10, 600 pp. 9707-9714, 1981.

- ~~Liu, A. Z.: Estimate eddy diffusion coefficients from gravity wave vertical momentum and heat fluxes, Geophys. Res. Let., Vol. 36, L08806, doi:10.1029/2009GL037495, 2009.~~
- Liu, G. and Shepherd, G. G.: An empirical model for the altitude of the OH nightglow emission, Geophys. Res. Let., Vol. 33, L09805, doi:10.1029/2005GL025297, 2006.
- 605 Lübken, F.-J., von Zahn, U., Thrane, E. V., Blix, T., Kokin, G. A., and Pachomov, S. V.: In situ measurements of turbulent energy dissipation rates and eddy diffusion coefficients during MAP/WINE, J. Atmos. Terr. Phys., Vol. 49, Nos. 7/8, pp. 763-775, 1987.
- Lübken, F.-J.: Seasonal variation of turbulent energy dissipation rates at high latitudes as determined by in situ measurements of neutral density fluctuations, J. Geophys. Res., Vol. 102, No. D12, pp. 13441-13456, 1997.
- 610 ~~Lübken, F.-J., Rapp, M. and Hofmann, P.: Neutral air turbulence and temperatures in the vicinity of polar mesospheric summer echoes, J. Geophys. Res., 107, D15, https://doi.org/10.1029/2001JD000915, 2002.~~
- Marsh, D. R.: Chemical-Dynamical Coupling in the Mesosphere and Lower Thermosphere, Aeronomy of the Earth's Atmosphere and Ionosphere (eds. Abdu, M. A. and Pancheva, D., Coed. Bhattacharyya, A.), IAGA Special Sopron Book Series 2, doi:10.1007/978-94-007-0326-1_1, Springer Science+Business Media B. V., 2011.
- 615 Moreels, G., Clairemidi, J., Faivre, M., Mougine-Sisini, D., Kouahla, M. N., Meriwether, J. W., Lehmacher, G. A., Vidal, E., and Veliz, O.: Stereoscopic imaging of the hydroxyl emissive layer at low latitudes, Planet. Space Sci., 56, pp. 1467-1479, 2008.
- Mulligan, F.J., Horgan, D.F., Galligan, J.G., Griffin, E.M.: Mesopause temperatures and integrated band brightnesses calculated from airglow OH emissions recorded at Maynooth (53.21N, 6.41W) during 1993. Journal of Atmospheric and Terrestrial Physics 57 (13), 1623–1637, 1995.
- 620 Nakamura, T., Higashikawa, A., Tsuda, T., and Matsuhita, Y.: Seasonal variations of gravity wave structures in OH airglow with a CCD imager at Shigaraki, Earth Planets Space, 51, 897-906, 1999. Offermann, D., Gusev, O., Donner, M., Forbes, J. M., Hagan, M., Mlynczak, M. G., Oberheide, J., Preusse, P., Schmidt, H., and Russell III, J. M.: Relative intensities of middle atmosphere waves, J. Geophys. Res., 114, D06110, doi:10.1029/2008JD010662, 2009.
- 625 ~~NASA National Space Science Data Center: COSPAR International Reference Atmosphere (CIRA 86): Global compilations of ground based, radiosonde, NIMBUS satellite and MSIS 86 model data from 1963–1973, NCAS British Atmospheric Data Centre, available at: https://catalogue.ceda.ac.uk/uuid/d758b820b4eba646ff0d6e05b552e23d (last access: 22 September 2020), 2007.~~
- Offermann, D., Gusev, O., Donner, M., Forbes, J. M., Hagan, M., Mlynczak, M. G., Oberheide, J., Preusse, P., Schmidt, H., and Russel III, J. M.: Relative intensities of middle atmosphere waves, J. Geophys. Res., Vol. 114, D06110, doi:10.1029/2008JD010662, 2009.
- 630 Pautet, P. D., Taylor, M. J., Pendleton, W. R., Zhao, Y., Yuan, T., Esplin, R., & McLain, D.: Advanced mesospheric temperature mapper for high-latitude airglow studies, Appl. Opt., 53(26), 5934-5943, 2014.
- Peterson, A. W.: Airglow events visible to the naked eye, Appl. Optics, 18, 3390–3393, doi:10.1364/AO.18.003390, 1979.

- 635 Peterson, A. W. and Kieffaber, L. M.: Infrared Photography of OH Airglow Structures, *Nature*, Vol. 242, pp. 321-322, 1973.
- ~~Prölss, G.: Physik des erdnahen Weltraums: Eine Einführung. Springer Verlag, Ausgabe 2, ISBN 3642188079, 9783642188077, 2001.~~
- Reisin, E.R., and Scheer, J.: Vertical propagation of gravity waves determined from zenith observations of airglow. *Adv. Space Res.*, Vol. 27, 1743–1748, 2001.
- 640 Satomura, T. and Sato, K.: Secondary generation of gravity waves associated with the breaking of mountain waves, *J. Atmos. Sci.*, 56, pp. 3847-3858, 1999.
- Schmidt, C., Höppner, K., and Bittner, M.: A ground-based spectrometer equipped with an InGaAs array for routine observations of OH(3-1) rotational temperatures in the mesopause region, *J. Atmos. Sol.-Terr. Phys.*, 102, pp. 125-139, 2013.
- 645 Schmidt, C., Dunker, T., Lichtenstern, S., Scheer, J., Wüst, S., Hoppe, U.-P., and Bittner, M.: Derivation of vertical wavelengths of gravity waves in the MLT-region from multispectral airglow observations, *J. Atmos. Sol.-Terr. Phys.*, 173, pp. 119-127, 2018.
- Sedlak, R., Hannawald, P., Schmidt, C., Wüst, S., and Bittner, M.: High-resolution observations of small-scale gravity waves and turbulence features in the OH airglow layer, *Atmos. Meas. Tech.*, 9, pp. 5955-5963, doi: 10.5194/amt-9-5955-2016, 2016.
- 650 Sedlak, R., Zuhr, A., Schmidt, C., Wüst, S., Bittner, M., Didebulidze, G. G., and Price, C.: Intra-annual variations of spectrally resolved gravity wave activity in the UMLT region, *Atmos. Meas. Tech.*, 13, pp. 5117-5128, <https://doi.org/10.5194/amt-2020-13-5117-2020>, 2020.
- Silber, I., Price, C., Schmidt, C., Wüst, S., Bittner, M., and Pecora, E.: First ground-based observations of mesopause temperatures above the Eastern-Mediterranean Part I: multi-day oscillations and tides, *J. Atmos. Sol.-Terr. Phys.*, 155, 95-103, 2017.
- 655 Smith, S., Baumgardner, J., and Mendillo, M.: Evidence of mesospheric gravity-waves generated by orographic forcing in the troposphere, *Geophys. Res. Lett.*, Vol. 36, 2009.
- Taylor, M. J.: A review of advances in imaging techniques for measuring short period gravity waves in the mesosphere and lower thermosphere, *Adv. Space Res.*, 19, pp. 667-676, 1997.
- 660 Taylor, M. J. and Hapgood, M. A.: On the origin of ripple-type wave structure in the OH nightglow emission, *Planet. Space Sci.*, 38, 1421–1430, 1990.
- Tuan, T. F., Hedinger, R., Silverman, S. M., and Okuda, M.: On gravity wave induced Brunt-Vaisala oscillations, *J. Geophys. Res.: Space Phys.*, Vol. 84, A2, pp. 393-398, 1979.
- 665 Vadas, S. L. and Fritts, D. C.: Gravity wave radiation and mean responses to local body forces in the atmosphere, *J. Atmos. Sci.*, Vol. 58, Issue 16, pp. 2249-2279, doi:10.1175/1520-0469(2001)058, 2001.
- Vadas, S.L., J. Zhao, X. Chu and E. Becker: The Excitation of secondary gravity waves from local body forces: Theory and observation, *J. Geophys. Res. Atmospheres*, 123, <https://doi.org/10.1029/2017JD027970>, 2018.

- 670 Vadas, S. L. and Becker, E.: Numerical Modeling of the Excitation, Propagation, and Dissipation of Primary and Secondary Gravity Waves during Wintertime at McMurdo Station in the Antarctic, *J. Geophys. Res.: Atmospheres*, 123, pp. 9326-9369, 2018.
- Wachter, P., Schmidt, C., Wüst, S., and Bittner, M.: Spatial gravity wave characteristics obtained from multiple OH(3-1) airglow temperature time series, *J. Atmos. Sol.-Terr. Phys.*, 135, pp. 192-201, 2015.
- ~~Weinstock, J.: Vertical Turbulent Diffusion in a Stably Stratified Fluid, *J. Atmos. Sci.*, Vol. 35, pp. 1022-1027, 1978.~~
- 675 Wüst, S., Wendt, V., Schmidt, C., Lichtenstern, S., Bittner, M., Yee, J.-H., Mlynczak, M. G., and Russell III, J. M.: Derivation of gravity wave potential energy density from NDMC measurements, *J. Atmos. Sol.-Terr. Phys.*, 138, 32–46, <https://doi.org/10.1016/j.jastp.2015.12.003>, 2016.
- Wüst, S., Schmidt, C., Bittner, M., Silber, I., Price, C., Yee, J.-H., Mlynczak, M. G., and Russel III, J. M.: First ground-based observations of mesopause temperatures above the Eastern-Mediterranean Part II: OH*-climatology and gravity wave activity, *J. Atmos. Sol.-Terr. Phys.*, 155, 104-111, 2017a.
- 680 Wüst, S., Bittner, M., Yee, J.-H., Mlynczak, M. G., and Russell III, J. M.: Variability of the Brunt–Väisälä frequency at the OH* layer height, *Atmos. Meas. Tech.*, 10, 4895–4903, <https://doi.org/10.5194/amt-10-4895-2017>, 2017b.
- Wüst, S., Offenwanger, T., Schmidt, C., Bittner, M., Jacobi, C., Stober, G., Yee, J.-H., Mlynczak, M. G., and Russell III, J. M.: Derivation of gravity wave intrinsic parameters and vertical wavelength using a single scanning OH(3-1) airglow spectrometer, *Atmos. Meas. Tech.*, 11, 2937–2947, <https://doi.org/10.5194/amt-11-2937-2018>, 2018.
- 685 Wüst, S., Schmidt, C., Hannawald, P., Bittner, M., Mlynczak, M. G., Russell III, J. M.: Observations of OH-airglow from ground, aircraft, and satellite: investigation of wave-like structures before a minor stratospheric warming. *Atmos. Phys. Chem.*, 19, 6401–6418, DOI: 10.5194/acp-19-6401-2019, 2019.
- Wüst, S., Bittner, M., Yee, J.-H., Mlynczak, M. G., and Russell III, J. M.: Variability of the Brunt–Väisälä frequency at the OH*-airglow layer height at low and midlatitudes, *Atmos. Meas. Tech.*, 13, 6067–6093, <https://doi.org/10.5194/amt-13-6067-2020>, 2020.
- 690 Yuan, T., She, C.-Y., Krueger, D. A., Sassi, F., Garcia, R., Roble, R. G., Liu, H.-L., and Schmidt, H.: Climatology of mesopause region temperature, zonal wind, and meridional wind over Fort Collins, Colorado (41° N, 105° W), and comparison with model simulations, *J. Geophys. Res.*, 113, D03105, <https://doi.org/10.1029/2007JD008697>, 2008.

695

Figures

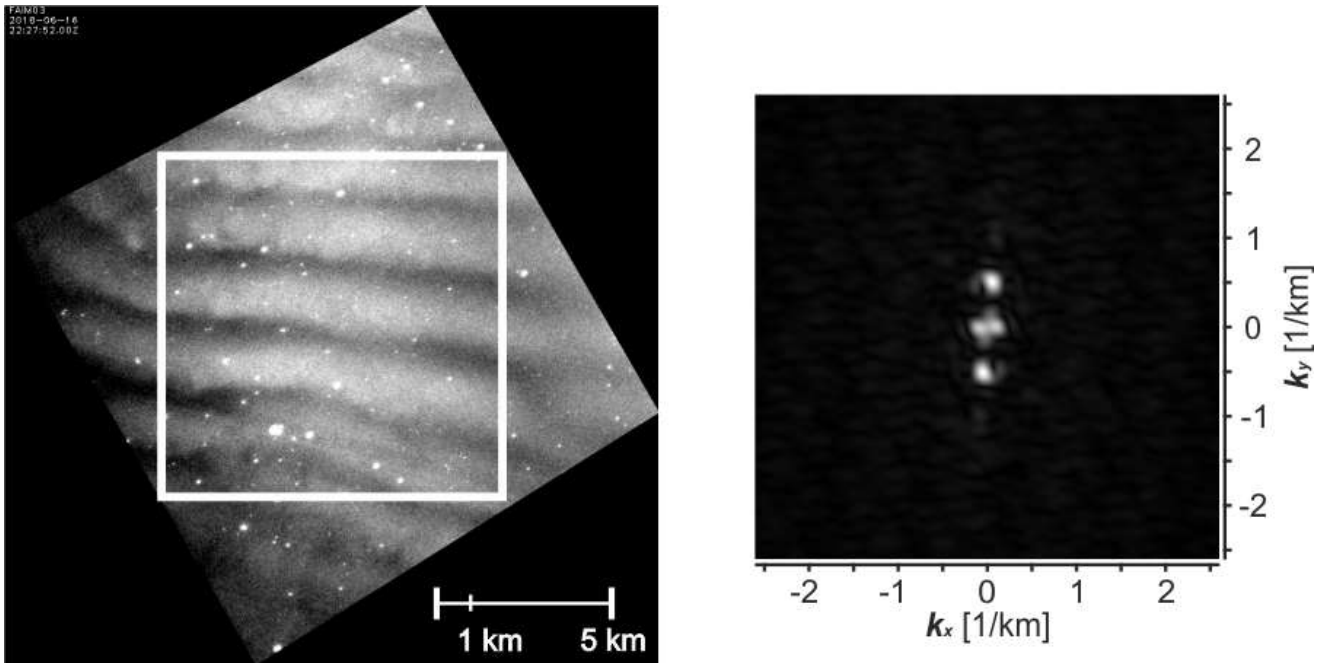


Figure 1. Event from 16 June 2018 22:27:52 UTC. The structure has a horizontal ‘wavelength’ of ca. 1.9km and extends over the entire image (left). The white square marks the area which is analysed with the 2d-FFT. The respective 2-dimensional spectrum is shown on the right-hand side in the k-space.

700

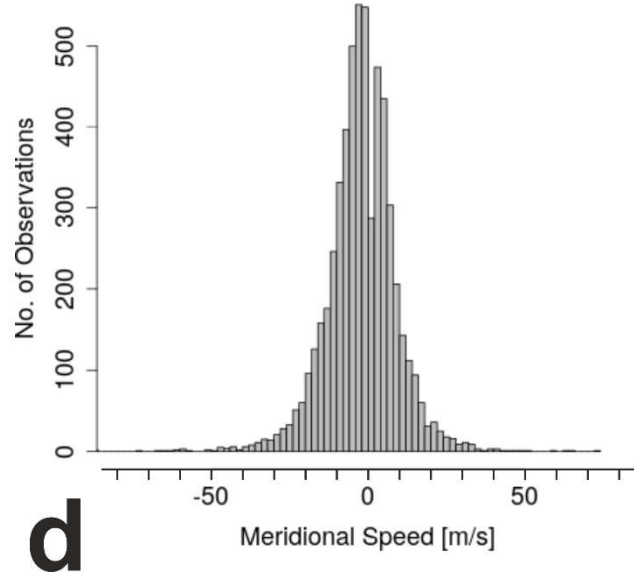
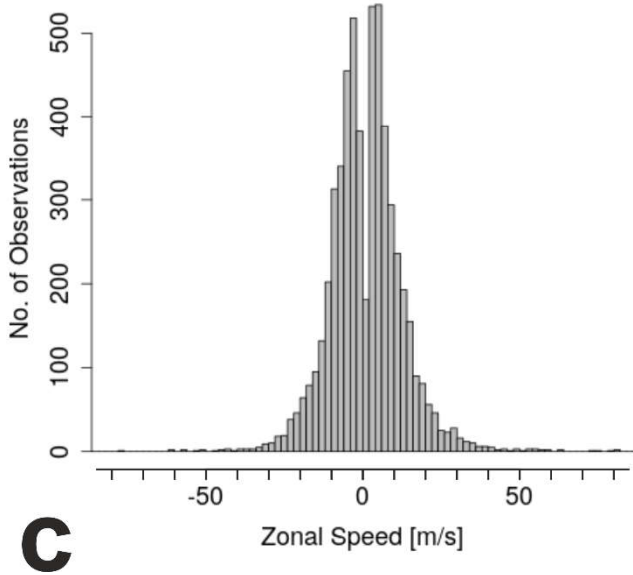
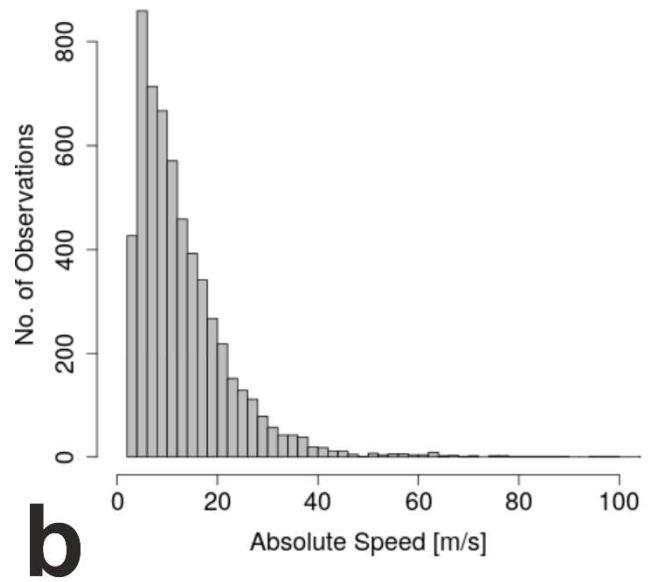
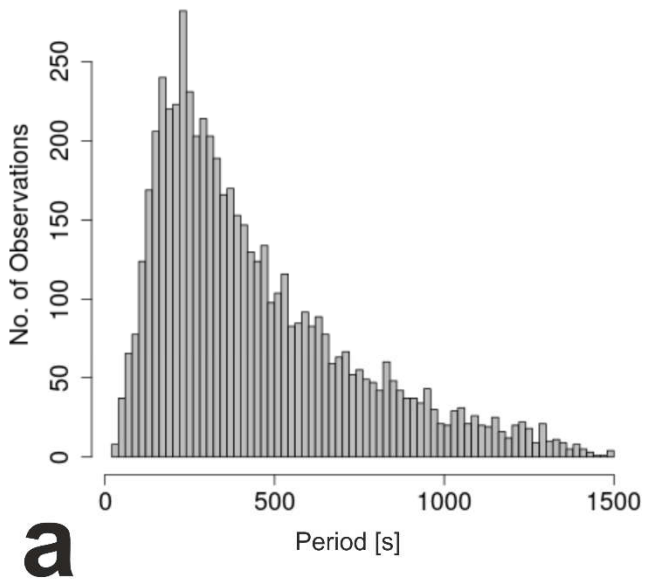


Figure 24. Statistical distribution of observed parameters for wave events with horizontal wavelengths between 48 m and 4.5 km from 26 October 2017 to 6 June 2019 at Otlica, Slovenia. ~~The contribution of wave events with a period longer than the respective BV period is coloured in grey.~~ a) Period. b) Absolute horizontal phase speed. c) Zonal phase speed. d) Meridional phase speed.

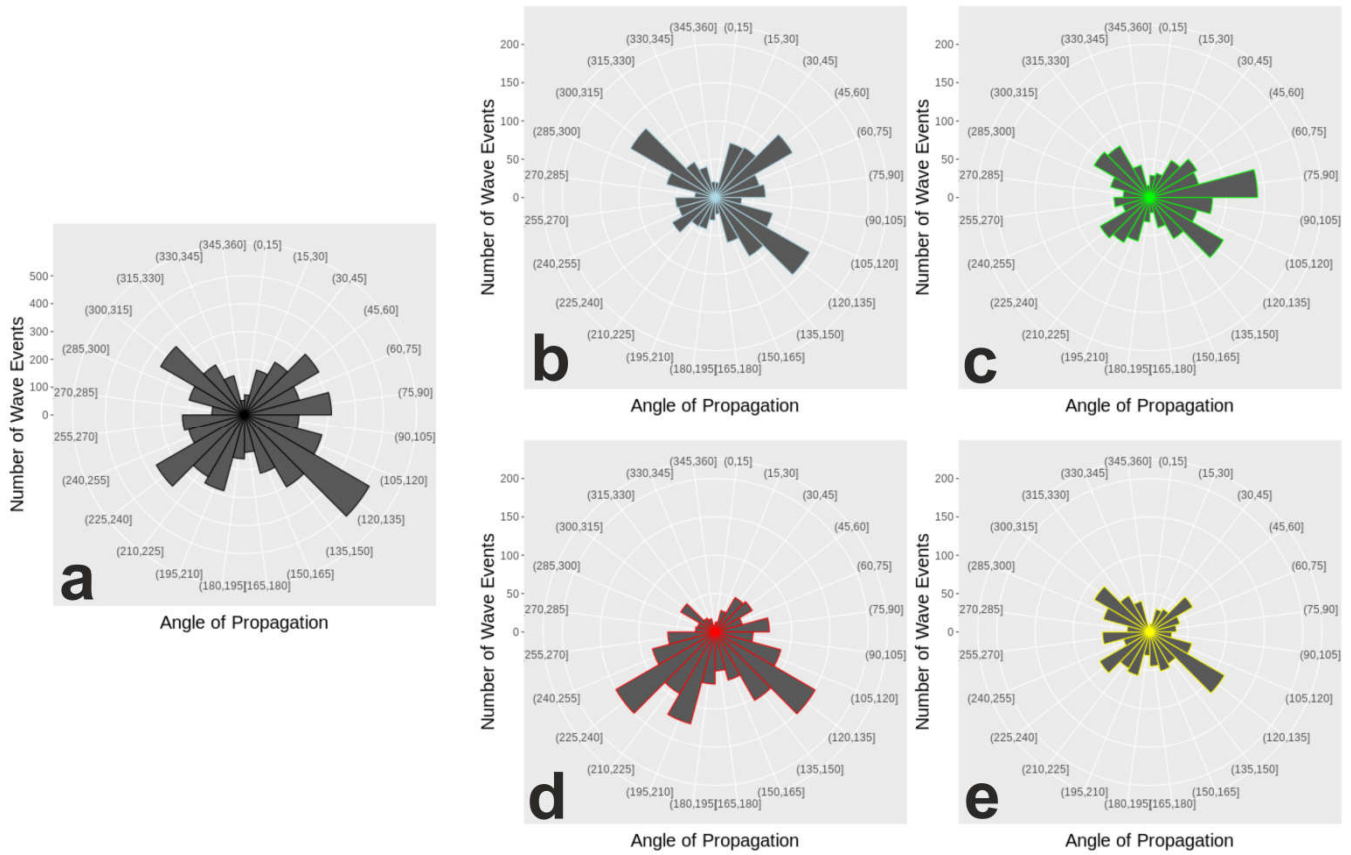
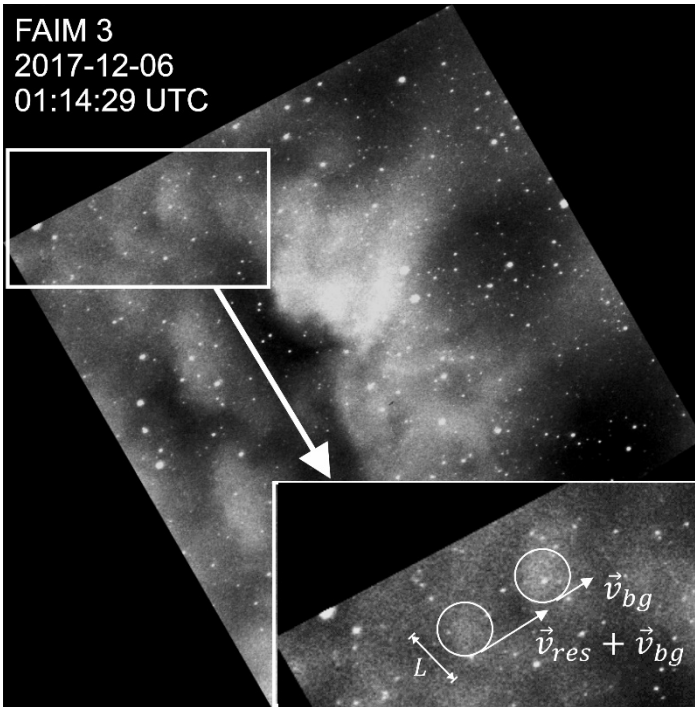
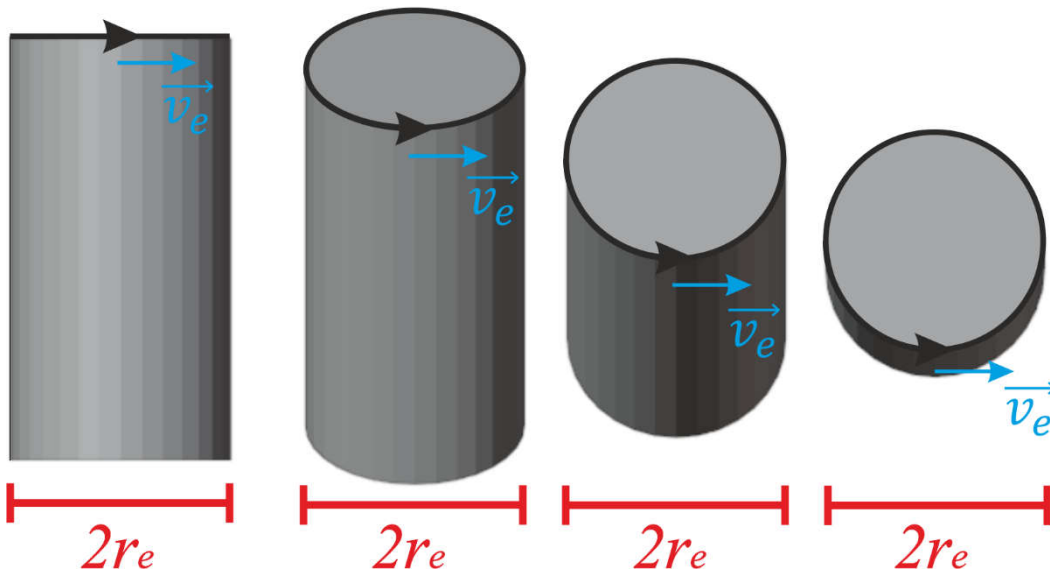


Figure 32. Statistical distribution of observed directions of propagation for wave events with horizontal wavelengths between 48 m and 4.5 km from 26 October 2017 to 6 June 2019 at Otlica, Slovenia. a) All. b) Winter (Dec-Jan-Feb). c) Spring (Mar-Apr-May). d) Summer (Jun-Jul-Aug). e) Autumn (Sep-Oct-Nov).

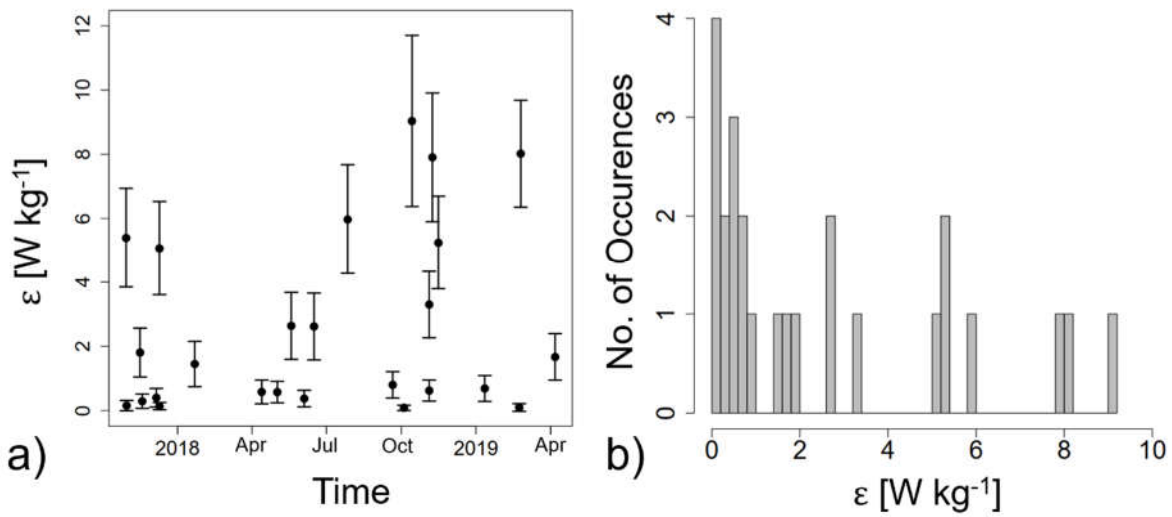


710 Figure 43. (a) Snapshot (1901:3614:41-29 UTC) of the turbulence episode from ~~64 November-December~~2018 between 19:32:24 and
 715 ~~19:40:59~~UTC. Two patches move in the same directions but have different speeds and are approaching each other. While the feature on the right-hand side seems to be advected by the wind (as do the structures in the entire image) the feature on the left-hand side moves even faster and belongs to those structures that creates the impression of turbulent dynamics. The latter patch moves with the residual velocity that is used in equation (1) plus the background velocity. The length scale L used in equation (1) is given by the size of this feature. he rotational axis (black line) and movement (red arrows) of a vortex are marked in the picture and on a cylinder (b) to guide the eye. This rotation of the vortex is more apparentturbulent episode is attached as in the video supplement to this article (Video 1)video 2 in the supplement of this article.



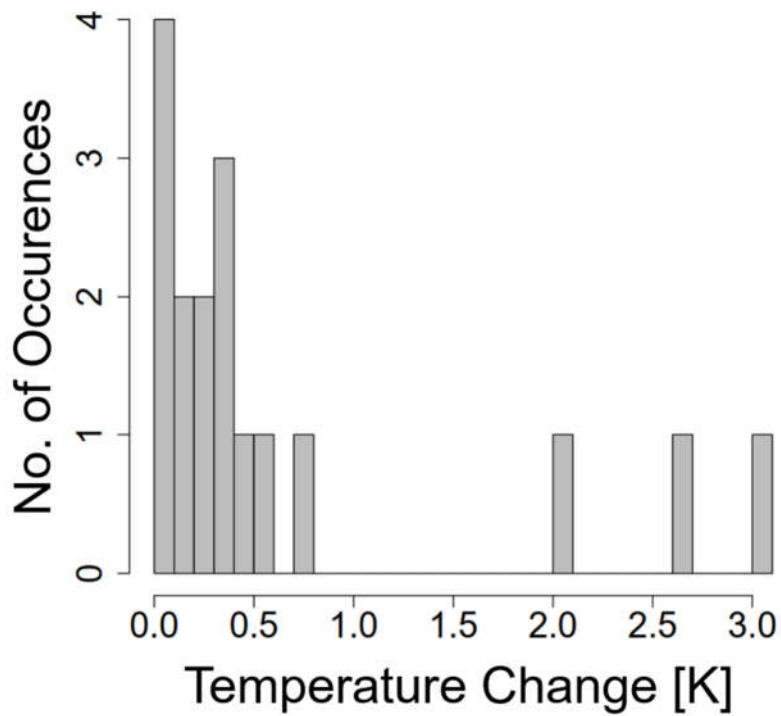
720

Figure 4. Schematic view of a rotating cylinder from different angles. In a 2-dimensional projection, the quantities we read from the images—the vortex radius r_e and the circumferential velocity v_e —remain the same for different perspectives.

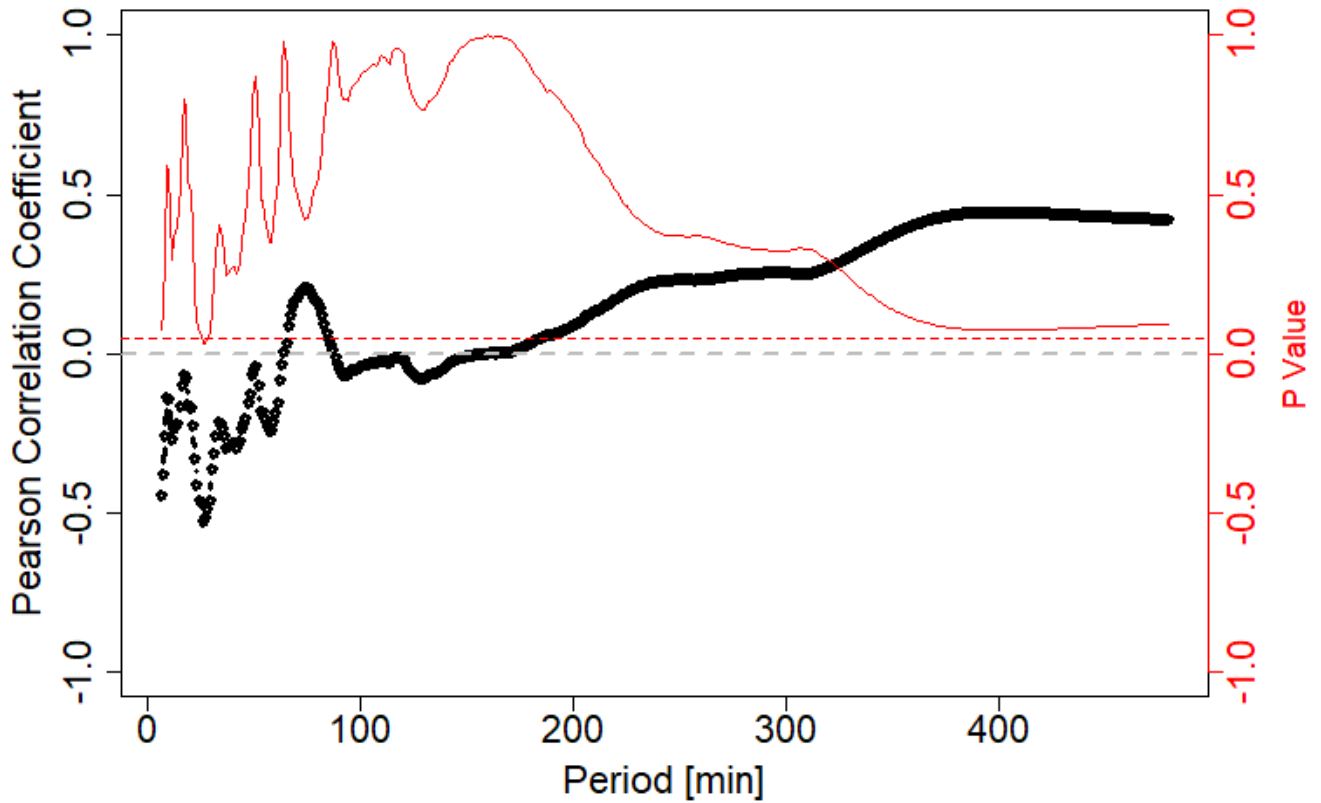


725

Figure 55. a) Temporal evolution of ~~eddy diffusion coefficients~~ energy dissipation (black) and energy dissipation rates (grey) of observed turbulence events at OTL (see Table 1). b) Histograms of ~~K and~~ ϵ .

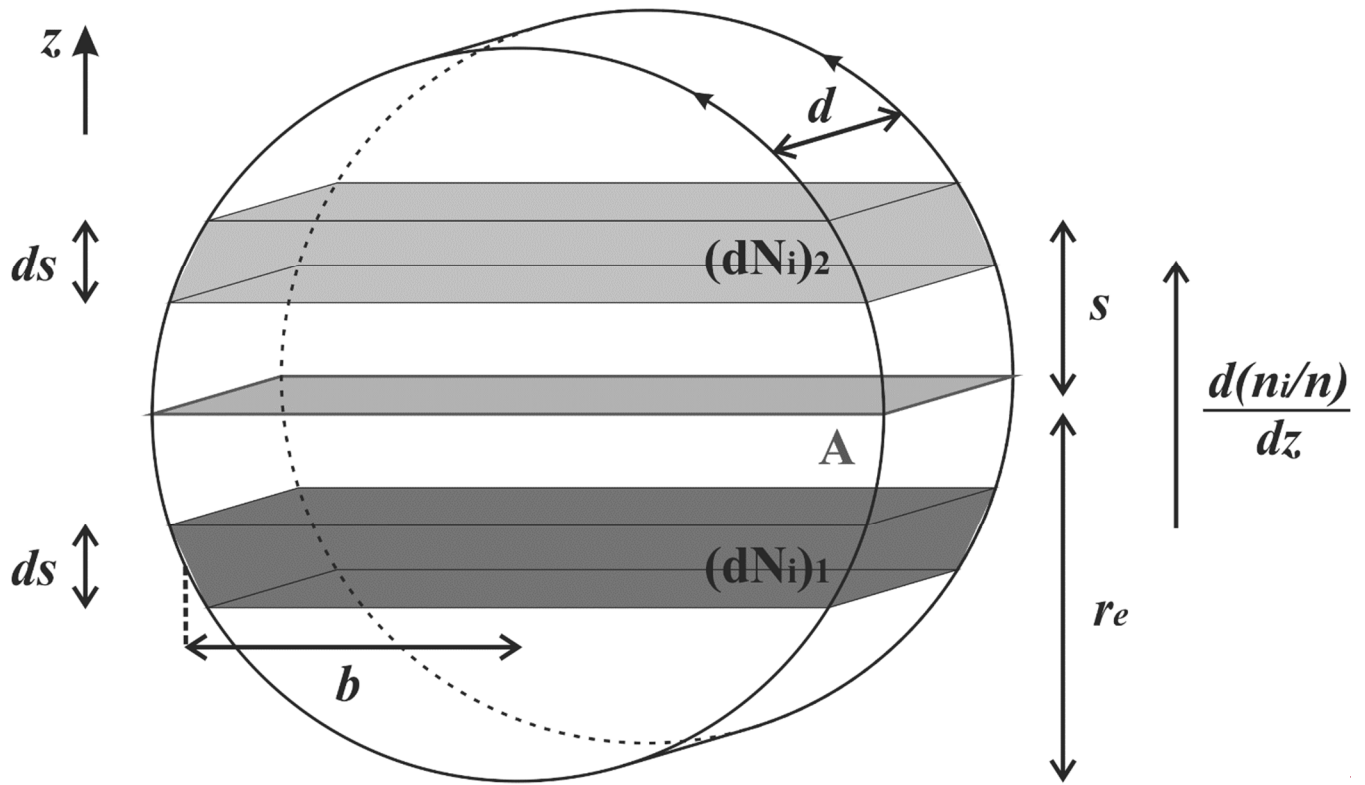


730 **Figure 66. a) Temporal evolution of dissipated energy per mass [J/kg] and respective temperature change [K] of observed turbulence events at OTL (see Table 1), assuming isobaric conditions and complete conversion of dissipated energy into heat. b) Histogram of dissipated energy per mass and temperature change resulting from the observed turbulence events assuming isobaric heating and full conversion into heat.**



735

Figure 77. Pearson correlation coefficient (black) between gravity wave activity (SWI) from GRIPS data and eddy diffusion coefficients from FAIM 3 data above OTL. The P value is plotted in red. For all P values of 0.05 (red horizontal line) or equal-less the correlation coefficient is considered significant. ~~A significant anticorrelation between SWI and the eddy diffusion coefficient is found between periods of 122 min and 207 min (grey vertical lines).~~



740 **Figure 8. Concept of cylindrical mixing according to Pröls (2001). Description in text.**

Tables

745

Table 1. Episodes of turbulence observed at OTL and derived parameters from the image sequences. **The BV frequency is according to the climatology based on TIMED SABER measurements as presented by Wüst et al. (2020).** The duration of the turbulence events could not be determined if the vortex was not visible during its entire life span due to being partly outside the FOV ('out of FOV') of FAIM 3 or covered by clouds ('clouds'). In these cases, we noted the dissipated energy per mass and the maximum temperature change as 'not available' (NA).

Date	DoY [d]	K [$10^4 \cdot \text{m}^2/\text{s}$]	Duration [s]	Angular BV frequency [$10^{-2} \cdot 1/\text{s}$]	ϵ [W/kg]	Diss. energy per mass [J/kg]	Max. temperature change [K]
2017-10-30	303	0.38 ± 0.08	out of FOV	2.10 ± 0.11	2.07 ± 0.63	NA	NA
2017-10-30	303	1.07 ± 0.13	244	2.10 ± 0.11	5.82 ± 1.31	1420 ± 319	1.4 ± 0.3
2017-11-01	305	0.27 ± 0.07	388	2.10 ± 0.11	1.48 ± 0.56	575 ± 217	0.6 ± 0.2
2017-11-16	320	0.17 ± 0.05	241	2.09 ± 0.10	0.91 ± 0.38	220 ± 92	0.2 ± 0.1
2017-11-18	322	0.54 ± 0.09	546	2.09 ± 0.10	2.90 ± 0.80	1585 ± 434	1.6 ± 0.4
2017-12-05	339	1.36 ± 0.15	373	2.09 ± 0.10	7.32 ± 1.56	2730 ± 583	2.7 ± 0.6
2017-12-06	340	0.33 ± 0.08	922	2.09 ± 0.10	1.79 ± 0.61	1655 ± 565	1.7 ± 0.6
2017-12-09	343	0.24 ± 0.08	407	2.09 ± 0.10	1.30 ± 0.57	530 ± 233	0.5 ± 0.2
2017-12-09	343	0.91 ± 0.13	390	2.09 ± 0.10	4.94 ± 1.20	1925 ± 469	1.9 ± 0.5
2018-01-22	22	0.84 ± 0.12	387	2.08 ± 0.10	4.53 ± 1.11	1752 ± 430	1.8 ± 0.4
2018-02-05	36	0.70 ± 0.11	146	2.07 ± 0.10	3.69 ± 0.93	538 ± 135	0.5 ± 0.1
2018-03-24	83	1.56 ± 0.16	250	2.11 ± 0.11	8.61 ± 1.75	2153 ± 437	2.2 ± 0.4
2018-04-12	102	0.70 ± 0.11	252	2.19 ± 0.11	4.16 ± 1.04	1048 ± 262	1.0 ± 0.3
2018-04-21	111	1.69 ± 0.17	292	2.23 ± 0.11	10.36 ± 2.08	3026 ± 608	3.0 ± 0.6
2018-04-29	119	0.96 ± 0.13	458	2.27 ± 0.11	6.09 ± 1.41	2787 ± 645	2.8 ± 0.6
2018-05-02	122	0.26 ± 0.08	531	2.28 ± 0.11	1.70 ± 0.67	905 ± 358	0.9 ± 0.4
2018-05-20	140	1.05 ± 0.13	out of FOV	2.37 ± 0.12	7.26 ± 1.64	NA	NA
2018-05-31	151	0.16 ± 0.06	309	2.42 ± 0.12	1.13 ± 0.55	349 ± 169	0.3 ± 0.2
2018-06-02	153	0.47 ± 0.09	413	2.42 ± 0.12	3.39 ± 1.00	1401 ± 414	1.4 ± 0.4
2018-06-04	155	0.22 ± 0.06	677	2.43 ± 0.12	1.63 ± 0.62	1102 ± 418	1.1 ± 0.4
2018-06-16	167	0.20 ± 0.06	291	2.46 ± 0.12	1.50 ± 0.58	437 ± 170	0.4 ± 0.2
2018-06-18	169	0.32 ± 0.15	382	2.47 ± 0.12	2.38 ± 1.11	908 ± 423	0.9 ± 0.4
2018-07-04	185	0.40 ± 0.08	340	2.48 ± 0.12	3.05 ± 0.94	1039 ± 320	1.0 ± 0.3
2018-07-25	206	0.33 ± 0.13	out of FOV	2.44 ± 0.12	2.42 ± 1.21	NA	NA
2018-07-28	209	1.94 ± 0.18	444	2.44 ± 0.12	14.21 ± 2.78	6309 ± 1233	6.3 ± 1.2
2018-09-21	264	1.90 ± 0.19	out of FOV	2.20 ± 0.11	11.34 ± 2.25	NA	NA

2018-09-21	264	0.13 ± 0.11	out of FOV	2.20 ± 0.11	0.78 ± 0.69	NA	NA
2018-10-02	275	0.23 ± 0.08	out of FOV	2.16 ± 0.11	1.31 ± 0.62	NA	NA
2018-10-04	277	0.59 ± 0.10	276	2.15 ± 0.11	3.38 ± 0.90	932 ± 248	0.9 ± 0.2
2018-10-04	277	0.86 ± 0.12	345	2.15 ± 0.11	4.95 ± 1.17	1709 ± 405	1.7 ± 0.4
2018-10-13	286	1.24 ± 0.15	914	2.13 ± 0.11	6.94 ± 1.50	6346 ± 1375	6.3 ± 1.4
2018-10-14	287	1.35 ± 0.16	out of FOV	2.13 ± 0.11	7.55 ± 1.63	NA	NA
2018-11-04	308	1.23 ± 0.15	915	2.09 ± 0.10	6.66 ± 1.45	6097 ± 1331	6.1 ± 1.3
2018-11-04	308	0.30 ± 0.08	609	2.09 ± 0.10	1.61 ± 0.61	983 ± 372	1.0 ± 0.4
2018-11-08	312	0.68 ± 0.10	out of FOV	2.09 ± 0.10	3.69 ± 0.93	NA	NA
2018-11-08	312	0.55 ± 0.09	out of FOV	2.09 ± 0.10	2.99 ± 0.80	NA	NA
2018-11-16	320	0.12 ± 0.12	out of FOV	2.09 ± 0.10	0.63 ± 0.70	NA	NA
2018-11-16	320	0.92 ± 0.13	292	2.09 ± 0.10	4.97 ± 1.19	1450 ± 346	1.4 ± 0.3
2019-01-11	11	0.57 ± 0.11	421	2.10 ± 0.11	3.08 ± 0.93	1297 ± 392	1.3 ± 0.4
2019-02-22	53	1.07 ± 0.14	318	2.07 ± 0.10	5.64 ± 1.28	1794 ± 409	1.8 ± 0.4
2019-02-24	55	1.61 ± 0.16	out of FOV	2.07 ± 0.10	8.51 ± 1.70	NA	NA
2019-03-02	61	1.69 ± 0.17	306	2.07 ± 0.10	8.95 ± 1.77	2739 ± 543	2.7 ± 0.5
2019-03-30	89	0.31 ± 0.11	453	2.13 ± 0.11	1.75 ± 0.80	793 ± 364	0.8 ± 0.4
2019-04-07	97	1.28 ± 0.17	clouds	2.17 ± 0.11	7.39 ± 1.72	NA	NA
2019-05-09	129	0.39 ± 0.13	out of FOV	2.32 ± 0.12	2.56 ± 1.14	NA	NA

<u>Date</u>	<u>ϵ [W/kg]</u>	<u>Duration [s]</u>	<u>Diss. energy per mass [J/kg]</u>	<u>Max. temperature change [K]</u>
<u>2017-10-30</u>	<u>$5,39 \pm 1,55$</u>	<u>out of FOV</u>	<u>NA</u>	<u>NA</u>
<u>2017-10-30</u>	<u>$0,16 \pm 0,16$</u>	<u>244</u>	<u>38,12</u>	<u>0,04</u>
<u>2017-11-16</u>	<u>$1,80 \pm 0,76$</u>	<u>241</u>	<u>434,82</u>	<u>0,43</u>
<u>2017-11-18</u>	<u>$0,29 \pm 0,22$</u>	<u>546</u>	<u>158,92</u>	<u>0,16</u>
<u>2017-12-06</u>	<u>$0,40 \pm 0,29$</u>	<u>922</u>	<u>368,90</u>	<u>0,37</u>
<u>2017-12-09</u>	<u>$5,07 \pm 1,46$</u>	<u>407</u>	<u>2062,35</u>	<u>2,06</u>
<u>2017-12-09</u>	<u>$0,14 \pm 0,11$</u>	<u>390</u>	<u>54,62</u>	<u>0,05</u>
<u>2018-01-22</u>	<u>$1,45 \pm 0,70$</u>	<u>387</u>	<u>560,42</u>	<u>0,56</u>
<u>2018-04-13</u>	<u>$0,58 \pm 0,37$</u>	<u>252</u>	<u>146,24</u>	<u>0,15</u>
<u>2018-05-02</u>	<u>$0,57 \pm 0,33$</u>	<u>531</u>	<u>305,22</u>	<u>0,31</u>

<u>2018-05-20</u>	<u>2,63 ± 1,04</u>	<u>out of FOV</u>	<u>NA</u>	<u>NA</u>
<u>2018-06-04</u>	<u>0,37 ± 0,26</u>	<u>677</u>	<u>253,44</u>	<u>0,25</u>
<u>2018-06-16</u>	<u>2,61 ± 1,04</u>	<u>291</u>	<u>760,87</u>	<u>0,76</u>
<u>2018-07-28</u>	<u>5,97 ± 1,70</u>	<u>444</u>	<u>2651,59</u>	<u>2,65</u>
<u>2018-09-21</u>	<u>0,80 ± 0,41</u>	<u>out of FOV</u>	<u>NA</u>	<u>NA</u>
<u>2018-10-04</u>	<u>0,09 ± 0,08</u>	<u>345</u>	<u>29,87</u>	<u>0,03</u>
<u>2018-10-14</u>	<u>9,03 ± 2,67</u>	<u>out of FOV</u>	<u>NA</u>	<u>NA</u>
<u>2018-11-04</u>	<u>3,30 ± 1,03</u>	<u>915</u>	<u>3015,28</u>	<u>3,02</u>
<u>2018-11-04</u>	<u>0,62 ± 0,33</u>	<u>609</u>	<u>378,88</u>	<u>0,38</u>
<u>2018-11-08</u>	<u>7,91 ± 2,00</u>	<u>out of FOV</u>	<u>NA</u>	<u>NA</u>
<u>2018-11-16</u>	<u>5,24 ± 1,45</u>	<u>out of FOV</u>	<u>NA</u>	<u>NA</u>
<u>2019-01-11</u>	<u>0,69 ± 0,40</u>	<u>421</u>	<u>289,10</u>	<u>0,29</u>
<u>2019-02-22</u>	<u>0,10 ± 0,12</u>	<u>318</u>	<u>31,13</u>	<u>0,03</u>
<u>2019-02-24</u>	<u>8,02 ± 1,66</u>	<u>out of FOV</u>	<u>NA</u>	<u>NA</u>
<u>2019-04-07</u>	<u>1,67 ± 0,72</u>	<u>clouds</u>	<u>NA</u>	<u>NA</u>